Monthly Notices of the ROYAL ASTRONOMICAL SOCIETY

MNRAS **511,** 3618–3635 (2022) https://doi.org/10.1093/mnras/stac101
Advance Access publication 2022 January 14

ATOMS: ALMA three-millimeter observations of massive star-forming regions – VII. A catalogue of SiO clumps from ACA observations

Rong Liu [1,2]★ Tie Liu,[3,4]★ Gang Chen,[5]★ Hong-Li Liu [6] Ke Wang,[7] Jin-Zeng Li,[1] Chang Won Lee,[8,9] Xunchuan Liu,[3,10] Mika Juvela [11] Guido Garay,[12] Lokesh Dewangan [13] Archana Soam [14,23] Leonardo Bronfman,[12] Jinhua He,[12,15,16] Chakali Eswaraiah,[17] Si-Ju Zhang,[7] Yong Zhang [18] Feng-Wei Xu [7,10] L. Viktor Tóth [19] Zhi-Qiang Shen,[3] Shanghuo Li,[8] Yue-Fang Wu,[10] Sheng-Li Qin,[6] Zhiyuan Ren [1] Guoyin Zhang,[1] Anandmayee Tej,[20] Paul F. Goldsmith,[21] Tapas Baug,[22] Qiuyi Luo,[3] Jianwen Zhou[1,2] and Chang Zhang[1,2]

Affiliations are listed at the end of the paper

Accepted 2022 January 6. Received 2021 December 23; in original form 2021 November 15

ABSTRACT

To understand the nature of SiO emission, we conducted ACA observations of the SiO (2-1) lines toward 146 massive star-forming regions, as part of the ALMA Three-millimeter Observations of Massive Star-forming regions (ATOMS) survey. We detected SiO emission in 128 (87.7 per cent) sources and identified 171 SiO clumps, 105 of which are spatially separated from 3 mm continuum emission. A large amount of the SiO line profiles (60 per cent) are non-Gaussian. The velocity dispersion of the SiO lines ranges from 0.3 to 5.43 km s^{-1}. In 63 sources the SiO clumps are associated with HII regions characterized by H40α emission. We find that 68 per cent (116) of the SiO clumps are associated with strong outflows. The median velocity dispersion of the SiO line for outflow sources and non-outflow sources is 1.91 km s^{-1} and 0.99 km s^{-1}, respectively. These results indicate that outflow activities could be connected to strongly shocked gas. The velocity dispersion and [SiO]/[H^{13}CO$^+$] intensity ratio do not show any correlation with the dust temperature and particle number density of clumps. We find a positive correlation between the SiO line luminosity and the bolometric luminosity, implying stronger shock activities are associated with more luminous protoclusters. The SiO clumps in associations with HII regions were found to show a steeper feature in $L_{\rm SiO}/L_{\rm bol}$. The SiO line luminosity and the fraction of shocked gas have no apparent evidence of correlation with the evolutionary stages traced by luminosity to mass ratio ($L_{\rm bol}/M$).

Key words: ISM: clouds – ISM: jets and outflows – ISM: molecules – stars: formation – stars: massive – radio lines: ISM.

1 INTRODUCTION

As the main contributors of heavy elements and UV-photon radiation, massive stars play an important role in the evolution of interstellar medium (ISM). In the past decades, studies of massive star formation through multiwavelengths and high-resolution observations have made great achievements, but there are still difficulties in understanding the formation process because of large distances, short timescales, high extinction, and clustered environments (Zinnecker & Yorke 2007; Motte, Bontemps & Louvet 2018). The process of massive star formation itself can also provide strong feedback to the parent clouds and ISM by energetic jets and induced outflows. The jets and outflows interacting with the surrounding medium are ubiquitous at different evolutionary stages in high-mass star formation, such as infrared quiet, infrared bright, and Ultra-Compact (UC) HII stage (Churchwell 2002; Bally 2016; Li et al. 2019a). Thus studies of such shock activities can help us deepen understanding of the massive star formation processes.

A deep understanding of the properties of jets and outflows is crucial in answering the problems in massive star formation (Motte et al. 2018). Molecular lines are powerful tools to study the physical and chemical conditions and the feedback within massive star-forming regions (SFRs). Various molecular emissions trace different layers in the internal structure of massive clumps embedding high-mass stars (Csengeri et al. 2016). Rotational transitions of different molecules provide us temperatures, densities, UV fields, chemical abundances, and gas kinematics of the massive clumps. Molecules such as CO, SiO, SO, HCO$^+$, and CS are good tracers of jets and outflows (Bally 2016). In particular, due to little contamination from the quiescent gas, SiO emissions have been widely used to study shock activities induced by outflows.

Shocks are a universal phenomenon in SFRs. High velocity shocks ($v_{\rm S} \geq$ 20 km s^{-1}) are caused by powerful outflows and jets from massive young protostars (Qiu et al. 2007; Duarte-Cabral et al. 2014; Li et al. 2019b, 2020), while low velocity shocks ($v_{\rm S}$ < 10 km s^{-1}) could be associated with less powerful outflows (Lefloch et al. 1998), cloud–cloud collisions (Louvet et al. 2016) or large-scale gas inflows

★ E-mail: liu_rong@bao.ac.cn (RL); liutie@shao.ac.cn (TL); ddwhcg@cug.edu.cn (GC)

(Jiménez-Serra et al. 2010). SiO is an excellent tracer of shocks. In the shocked regions, grain material is destructed via sputtering or vaporization, leading the Si atoms and Si-bearing molecules to be injected into the gas phase and subsequently oxidized to SiO (Schilke et al. 1997; Gusdorf et al. 2008b). In active star-forming regions, SiO abundance is enhanced by up to six orders of magnitudes compared to quiescent regions (Martin-Pintado, Bachiller & Fuente 1992; Codella, Bachiller & Reipurth 1999). Observations of the SiO emission lines toward different sources exhibit a variety of profiles. Previous studies reported that the spectra of SiO usually shows two Gaussian components both corresponding to similar central velocities but different line widths, namely, the broad component and the narrow one (Martin-Pintado et al. 1992; Lefloch et al. 1998). These two SiO components trace different emission regions and may have different origins (Schilke et al. 1997). The broad components are thought to be related to high-velocity shocks from protostellar outflows, and the narrow components are attributed to low-velocity shocks linked to low-velocity motions (see above).

Based on studies targeting the variation of SiO emission toward different evolutionary stages of star formation, several studies found the brighter SiO emission are associated with higher luminosity sources (Codella et al. 1999; Liu et al. 2020c), which would be consistent with the trend that the SiO abundance in warmer sources is higher than the one in infrared-quiet sources (Gerner et al. 2014; Miettinen 2014). Motte et al. (2007) and Sakai et al. (2010) found that younger sources show brighter SiO emission than mid-infrared bright sources. The studies of Miettinen et al. (2006), López-Sepulcre et al. (2011), and Sánchez-Monge et al. (2013) are consistent with a decrease in SiO abundance in more evolved sources. The results that the SiO abundance have no trend among different evolutionary stages also have been reported by Sanhueza et al. (2012), Leurini et al. (2014), Csengeri et al. (2016), and Li et al. (2019a). Recently, Liu et al. (2021c) reported an increasing trend of the SiO line luminosity with bolometric luminosity, but they do not see the relation between the SiO line luminosity and the bolometric luminosity-to-mass ratio. So far, there is no consensus on SiO abundance variation in different evolutionary stages.

During the past decades, a large number of SiO studies toward massive star-forming regions have been conducted. The SiO abundance and excitation variations have been studied by searching for evolutionary trends in different samples (Codella et al. 1999; Miettinen et al. 2006; Motte et al. 2007; Sakai et al. 2010; Gerner et al. 2014; Csengeri et al. 2016; Li et al. 2019a; Liu et al. 2020c). Moreover, Jiménez-Serra et al. (2010), Duarte-Cabral et al. (2014), Louvet et al. (2016), and Cosentino et al. (2020) investigated the mechanisms responsible for the broad and narrow line profile of SiO. However, previous studies have been focused on either individual sources through interferometer arrays or large samples with single-dish observations. The origin of the SiO emission is still an enigma for astronomers without a high resolution survey of SiO emission toward a large sample of sources with interferometers.

The ALMA Three-millimeter Observations of Massive Star-forming regions (ATOMS) survey employed the Band 3 and covered eight spectral windows (two wide spectral windows in upper side band and six spectral windows in lower side band) toward 146 massive star-forming sources (Liu et al. 2020a). The survey provides us larger samples and high resolution to systemically study various molecular gas involved in star formation. In this paper, we statistically analyse SiO emission of 146 sources using the Atacama Compact 7 m Array observations (ACA) to better understand shocked gas under different conditions and in different evolutionary trends. We establish a catalogue of the SiO clumps for future studies. We present the level of shock activities and estimate the fraction of the shocked gas in the clumps. The paper is organized as follows: the sample selection and observations are presented in Section 2. Section 3 gives our results. We put discussion in Section 4 and summary in Section 5.

2 OBSERVATIONS

2.1 Sample

A sample of 146 massive SFRs from the ATOMS survey were investigated in this paper. The sample sources were selected from the CS $J = 2$-1 line survey of UC HII regions in the Galactic Plane (Bronfman, Nyman & May 1996). The sample sources are complete for protoclusters characterized by bright CS $J = 2$-1 emission ($T_b > 2$ K), implying reasonably dense gas. The basic parameters of the sample were taken from Liu et al. (2020a,b, 2021b; paper I, paper II, and paper III of the series). The distance of the sample sources ranges from 0.4 kpc to 13.0 kpc with a mean value of 4.5 kpc. The clump mass ranges from 5.6 to 2.5×10^5 $M_\odot$, with a median value of 1.4×10^3 $M_\odot$. The bolometric luminosity ranges from 16 to 8.1×10^6 $L_\odot$, with a median value of 5.7×10^4 $L_\odot$. The radii ranges from 0.06 to 4.26 pc, with a median value of 0.86 pc. The dust temperature ranges from 18 to 46 K, with a median value of 29 K.

2.2 ALMA Observations

The present study is based on the ATOMS survey data (Project ID: 2019.1.00685.S; PI: Tie Liu). The survey has collected both 12m-array and ACA data. We focus the latter in this work with an aim at compiling a complete catalogue of SiO emission clumps owing to the benefit from the large field of view of the ACA observations. The Atacama Compact 7 m Array (ACA) observations were conducted from 2019 September to mid-November. The typical ACA observing time is ∼8 min. The angular resolution of ACA observations is ∼13.1−13.8 arcsec and the maximum recovered angular scale is ∼53.8−76.2 arcsec. The SiO J = 2-1, HCO^+ J = 1-0, $H^{13}CO^+$ $J = 1$-0 lines are included in SPWs 1∼6 at the lower side band with the spectral resolutions of 0.21, 0.11, and 0.21 km s^{-1}, respectively (Liu et al. 2021b,a). The H40α and CS $J = 2$-1 lines are included in SPWs 7 at the upper side band with the spectral resolutions of 1.49 km s^{-1}. The ACA data were calibrated and imaged by CASA software package version 5.6 (McMullin et al. 2007), and more details about data reduction can be found in Paper I.

3 RESULTS

For the identification of SiO clumps, we firstly generate the integrated intensity (Moment 0) maps of SiO emission using channels with signals higher than 3σ. The rms level σ for each source are listed in Tables A1 and A2. In Moment-0 maps, we have identified 171 SiO clumps in 128 sources by eye. We identified SiO clumps by eye because there are not so many SiO clumps within individual sources and the emission peaks of most SiO clumps are clearly separated from each other in these low-resolution ACA images. Therefore, we did not apply any algorithm in clump identification in order to avoid fake detection close to the edges of images where the signal-to-noise levels are low. Then we used the two-dimensional fitting tools (*imfit*) in CASA to fit these SiO clumps one by one. We get deconvolved sizes (the full width at half maximum, FWHM, and position angle, PA), center positions and integrated intensity for these SiO clumps. SiO clumps in the marginal region are excluded. These results are shown

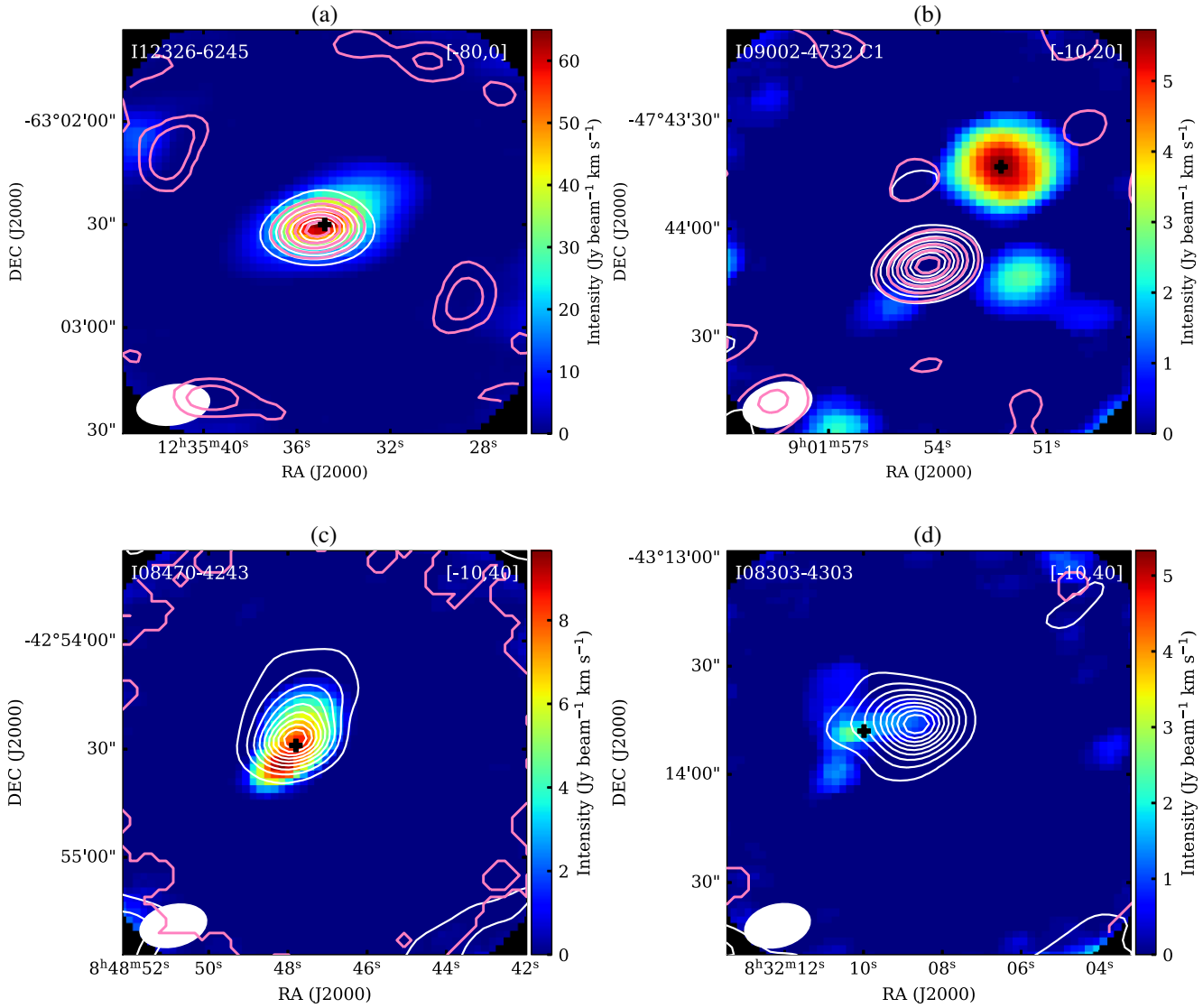

Figure 1. Example sources. The background is SiO (2-1) integrated intensity maps. The white contours are 3 mm continuum emission, and contours are from 10 per cent to 100 per cent in the step of 10 per cent of peak values. The pink contours represent H40α emission, contours from 10 per cent to 100 per cent in the step of 20 per cent of peak values. The source name is shown on the upper left. The black cross is the central position extracted spectra and the beam size is presented at the lower left corner. The integration ranges are shown in the upper right corner. (A) Panel presents source associated with 3 mm emission and coincided with H40α emission. (B) Panel shows source separated with 3 mm emission and coincided with H40α emission. (C) Panel presents source associated with 3mm emission undetected H40α emission. (D) Panel shows source separated with 3mm emission undetected H40α emission. All images have a field of view of $2'2'$.

in Tables A1 and A2. Next we extract the spectra of SiO lines toward the peak positions of SiO clumps in all detected sources. The spectra were extracted over the aperture of clumps size or beam size (clumps smaller than the beam size). Examples of the Moment-0 maps and spectra are shown in Appendix A1.

Fig. 1 shows four examples of detected sources. A Moment-0 map of SiO emission overlaid by contours of 3 mm continuum emission and H40α emission is shown. We classify the sources into four groups based on their different conditions in line emission. The classification criteria are as follows:

(A) 27 SiO clumps in sources containing HII regions: SiO emission associated with both H40α emission and 3 mm continuum emission.

(B) 59 SiO clumps in sources containing HII regions: SiO emission separated from both H40α emission and 3 mm continuum emission.

(C) 39 SiO clumps in sources containing non-HII regions: SiO emission associated with 3mm continuum emission.

(D) 46 SiO clumps in sources containing non-HII regions: SiO emission partly separated from 3mm continuum emission.

Fig. 2 present the SiO (2-1), HCO^+ (1-0), and CS (2-1) spectra extracted toward four exemplar SiO clumps. We smooth the spectral resolution of SiO and HCO^+ to the spectral resolution of CS (1.49 km s^{-1}) for comparison. In I12326-6245, I08470-4243, and I08303-4303, the spectra of SiO show high-velocity wings, and we can see two distinct components: a narrow component and a broad component. The broad SiO components especially with red- and/or blue-shifted line wings are likely related to molecular outflows. In I12326-6245, I08470-4243, and I08303-4303, the spectra of HCO^+ and CS also show high-velocity wings. In I09002-4732 C1, there

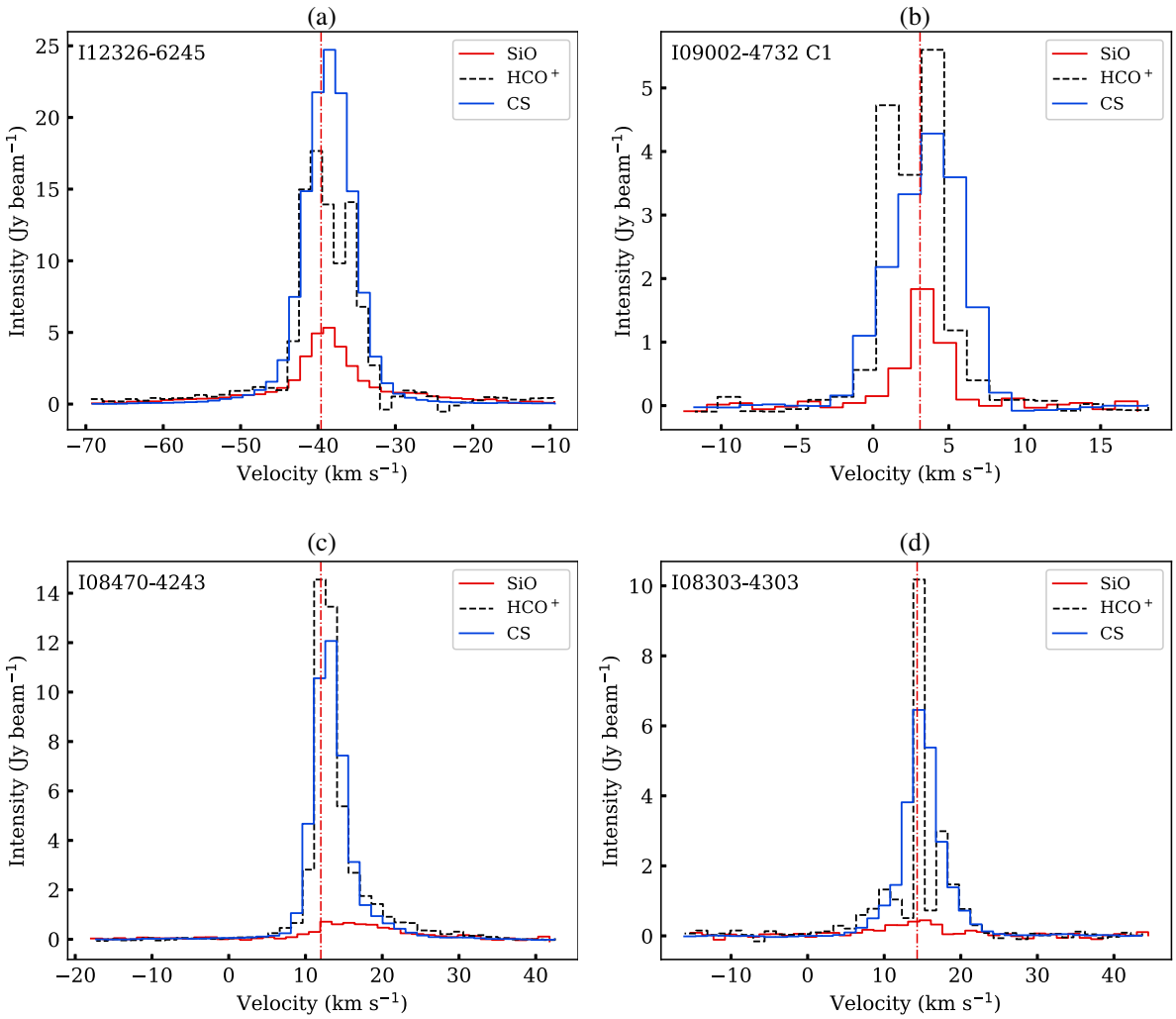

Figure 2. Examples of sources. The red spectrum represents the SiO average spectral extracted over the aperture of SiO clumps or beam. The HCO^+ and CS spectra are presented as black dashed and blue solid lines. The dash–dotted line indicates the systemic velocity of the source.

is no high-velocity wing emission in all lines, indicating that this source does not have outflows. The spectra of other SiO clumps are shown in Appendix A1.

In most detected SiO clumps, we can see the peak velocity of the narrow components is similar to the systemic velocity (marked by the red dash–dotted line). We thus consider these components coincided with the ambient cloud. In very rare cases such as I08076-3556 (Appendix A1), however, the SiO velocity (∼40 km s^{-1}) deviated clearly from the systemic velocity (5.9 km s^{-1}) and SiO line emission mainly comes from red-shifted line wings.

3.1 Detection rates of SiO emission

Toward the 146 sources, SiO (2-1) emission was detected in 128 (87.7 per cent) sources, indicating that the presence of shocks is very common in high-mass star-forming regions. In particular, when we inspect the spectra of the sources that do not show strong SiO emission in their Moment-0 maps, we find additional 18 SiO clumps showing weak SiO emission, with peak intensity close to 2σ. We list these weak SiO clumps in Table A2.

Because of the complicated and non-Gaussian SiO line profiles, we instead use their Moment-0 maps, the intensity-weighted velocity (Moment 1) maps, and the intensity-weighted velocity dispersion (Moment 2) maps to derive their velocity (v), and velocity dispersion (σ_V). The derived parameters of SiO clumps are summarized in Table A1. Notably, the velocity dispersion of SiO emission is mostly larger than the velocity resolution (0.21 km s^{-1}). For the 18 weaker clumps, we use one component Gaussian fit of their averaged spectra to get the line parameters (Intensity, velocity, and velocity dispersion). The derived line parameters are shown in Table A2.

3.2 The velocity dispersion of SiO and the line wings of SiO, HCO^+, and CS

The velocity dispersions of the detected SiO lines are listed in Tables A1 and A2. For the SiO lines, the range of the velocity dispersion values is 0.3∼5.43 km s^{-1}. The mean values is 1.77 km s^{-1}, and the median values is 1.59 km s^{-1}. The histogram of the velocity dispersion is presented in Fig. 3.

To identify strong outflows in these sources, we searched the line wings in SiO, HCO^+, and CS emission lines. These results are listed in Table A3. Because of relatively high abundance, HCO^+ emission is a very good tracer of outflows (Myers et al. 1996). Therefore, in outflow regions, HCO^+ emission is detectable even if SiO emission

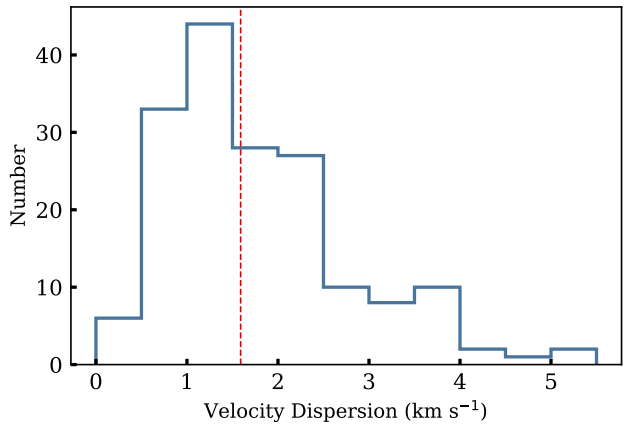

Figure 3. Histogram of the velocity dispersion of the SiO (2-1) lines. The vertical red dashed line represents the median velocity dispersion.

is not detected. However, in some sources the line profile of HCO^+ emission is self-absorbed. We inspect the spectra of CS and find its spectra to be less self-absorbed. As a consequence, we use the line wings of SiO, HCO^+, and CS together to identify strong outflows. The spectra of SiO, HCO^+, and CS are shown in Appendix A1. According to the high-velocity line wings, the SiO clumps are divided into two groups: clumps with strong outflows and without strong outflows. We find 116 clumps are associated with outflows showing wing emission in at least one of the three lines and 50 clumps are not associated with outflows. However, we cannot exclude these clumps without outflows that are not associated with weak outflows. We exclude I17441-2822 spectra in further analysis because this source is close to the Galactic center and shows very complicated line profiles.

3.3 SiO clumps properties

Using the Moment-0 maps of SiO emission, we have identified 171 SiO clumps. We calculated the geometric mean of the major axis FWHM and the minor axis FWHM and got the SiO clumps linear radius. The histogram of the SiO clump radii is presented in Fig. 4. The range of the SiO clump radii is 0.03∼0.99 pc. The mean value is 0.3 pc, and the median value is 0.23 pc. In addition, we failed to fit 116 clumps because the shape of SiO clumps is irregular and the size of these SiO clumps is smaller than or close to the beam size. Instead, we give the beam size as these clump sizes, and we marked these clumps in Table A1. The velocities of SiO clumps are approximately consistent with the systemic velocities of the clumps, except for I08076-3556 (Section 3).

In Moment-0 maps, we found that 105 SiO clumps are not spatially coincided with the peak of 3 mm continuum emission with separation

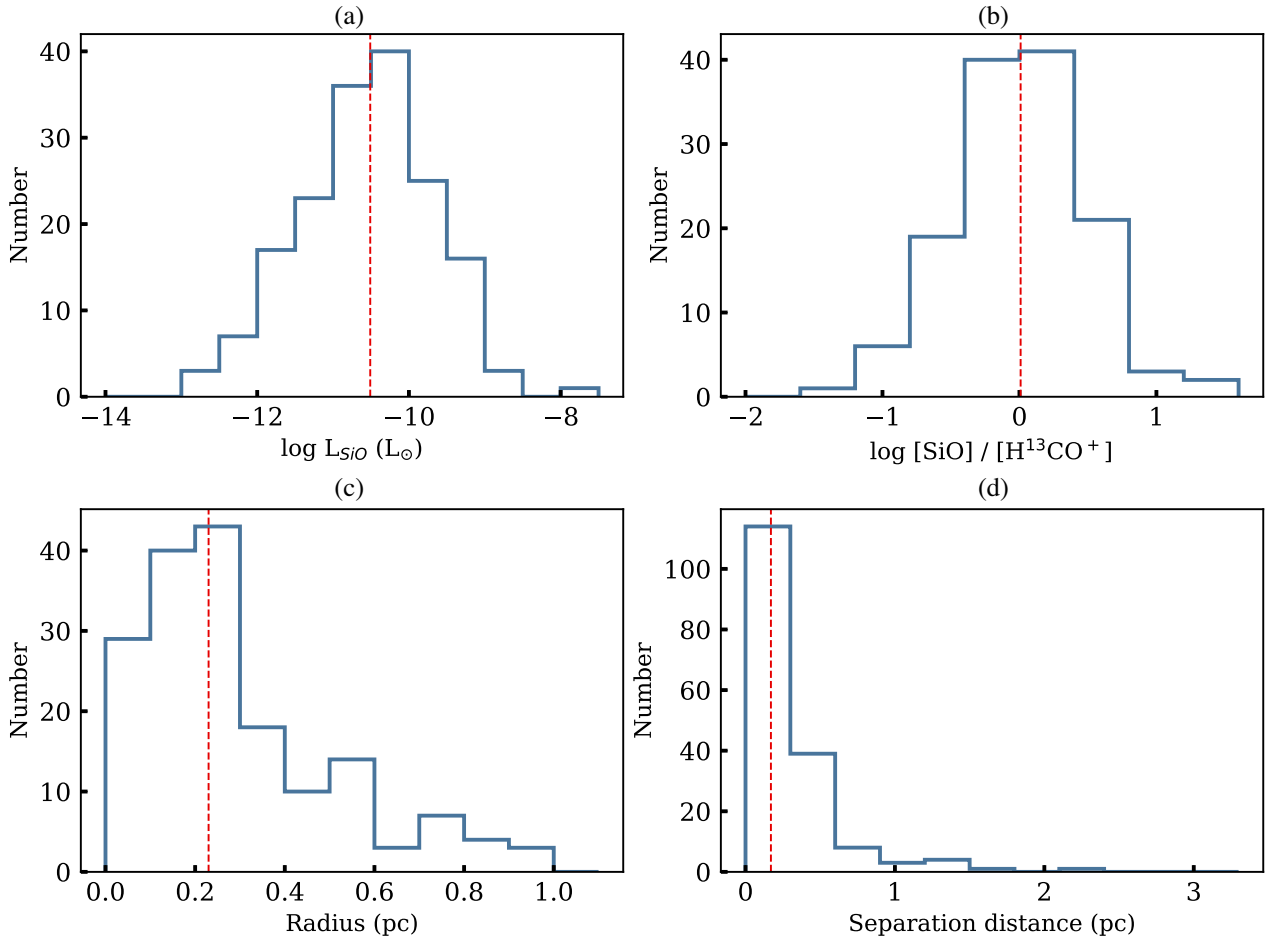

Figure 4. (a) Histogram of the SiO luminosity. (b) Histogram of the [SiO]/[$H^{13}CO^+$] ratio. (c) Histogram of separation distance. (d) Histogram of the SiO clump radius. The vertical red dashed line represents the median values of the parameter.

larger than half of beam size. There are 66 SiO clumps associated with 3 mm continuum emission. We derived the distances between the central positions of SiO clumps and the peak positions of the 3 mm continuum emission. These results are listed in Table A3. The histogram of the separation distance is presented in Fig. 4. The range of the separation is 0∼3.35 pc. The mean value is 0.3 pc, and the median value is 0.17 pc. An evident tail is presented in the separation histogram which represents these SiO clumps away from the 3 mm continuum emission may not be caused by outflows. This separation between the thermal dust and SiO molecular gas is similar to the results of López-Sepulcre et al. (2016) and Li et al. (2020).

For the 128 sources with SiO emission, 63 sources have H40α emission above 3σ. The H40α emission shows a compact structure and is coincident with the 3 mm continuum emission, indicating the existence of compact HII regions. For some of these sources, we find that SiO clumps are surrounding the H40α emission, indicating the possible existence of shocks induced by interaction between HII regions and their surrounding molecular clouds (Cosentino et al. 2020; Liu et al. 2020a). We will investigate the properties of shocked gas caused by HII regions using the high resolution 12-m array data in a forthcoming work.

We calculate the SiO (2-1) luminosity ($L_{\rm SiO}$) of the SiO clumps using the integrated intensity and the source distance. $L_{\rm SiO}$ can be derived from the formula:

$$L_{\rm SiO} = 4\pi \times d^2 \times \int F_\nu {\rm d}\nu, \quad (1)$$

where d is the distance to the source and ν represents the velocity. $\int F_\nu {\rm d}\nu$ is the integrated intensity of the SiO clump.

$L_{\rm SiO}$ from 1.74×10^{-13} to 1.07×10^{-8}L$_\odot$. The mean value is 2.69×10^{-11}L$_\odot$, and the median value is 3.1×10^{-11}L$_\odot$. Fig. 4 (a) shows the number distribution of the SiO luminosity. We used the sum $L_{\rm SiO}$ in one source for statistic analysis. More details on $L_{\rm SiO}$ will be discussed in Section 4.2.

3.4 The fraction of shocked gas

The $H^{13}CO^+$ emission is a good tracer of relatively quiescent gas. The $H^{13}CO^+$ abundance does not vary substantially with time (Nomura & Millar 2004). Therefore, column density of $H^{13}CO^+$ could reflect the dense gas of the clump. Sakai et al. (2010) used SiO column density against $H^{13}CO^+$ column density to represent the fraction of shocked gas in a dense clump. Assuming both SiO and $H^{13}CO^+$ emission are optically thin and have constant excitation temperatures, the integrated intensity ratios of SiO emission and $H^{13}CO^+$ emission can approximately reflect the relative fraction of the shocked gas in the clump, and later we use [SiO]/[$H^{13}CO^+$] to represent this ratio. The derived ratios are shown in Table A3. We inspected $H^{13}CO^+$ spectra and found that 12 sources have absorption features in their spectra. As a result, in the latter analysis, we ignore these 12 sources. For sources containing multiple SiO clumps, we calculate an average [SiO]/[$H^{13}CO^+$] ratio. The range of [SiO]/[$H^{13}CO^+$] is 0.04∼42.79. The mean values is 2.41, and the median values is 1.02. The histogram of [SiO]/[$H^{13}CO^+$] of all sources is presented in Fig. 4 (b).

4 DISCUSSION

4.1 The line broadening of SiO emission

The broad components of SiO emission in our sample are likely caused by the high-velocity gas driven by energetic outflows. The high detection rate of the velocity wings of SiO emission (60 per cent) suggests the presence of outflows. Our finding divides

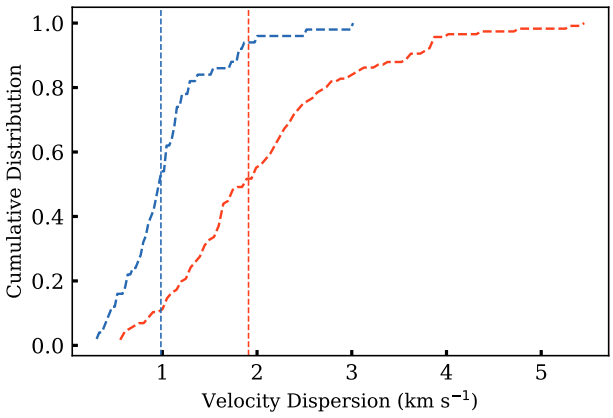

Figure 5. The velocity dispersion distributions for SiO clumps with outflows and without outflows (the red and blue lines). The vertical dashed lines represent the median velocity dispersion of SiO clumps in the two groups: 1.91 km s^{-1} (red line) and 0.99 km s^{-1} (blue line) for clumps with and without strong outflows, respectively.

the SiO clumps into two groups (Section 3.2). In the group with outflows, the median velocity dispersion of the SiO emission is as large as 1.91 km s^{-1}. In the other group without outflows, the narrow components of SiO emission are common and the median velocity dispersion of the SiO emission is 0.99 km s^{-1}. This narrow SiO emission could be created by unresolved low mass outflows, cloud–cloud collision, or gas inflows.

We plot the cumulative distribution of the SiO velocity dispersion for these two groups in Fig. 5. The SiO clumps with outflows are presented as red curve, while the clumps without outflows are shown as blue curve. For the SiO clumps with strong outflows, the velocity dispersion values range from 0.58 to 5.43 km s^{-1} with a mean value of 2.08 km s^{-1} and a standard deviation of 1.00 km s^{-1}. In contrast, for the SiO clumps without strong outflows, the velocity dispersion values are from 0.32 to 3 km s^{-1}, with a mean value of 1.06 km s^{-1} and a standard deviation of 0.53 km s^{-1}. In addition, we use the Kolmogorov–Smirnov (KS) test to compare these distributions. The P-value returned by the KS test is the probability that the two samples were drawn from the same distributions. If the P-value is smaller than 5 per cent, we conclude that the two samples were drawn from different distributions. The KS test gives a P-value of about 10^{-12}, indicating that the velocity dispersion distribution of these two groups is very different. The clumps associated with outflows show significantly larger velocity dispersion in SiO emission on average.

In shocked gas, the SiO velocity dispersion is attributed to non-thermal broadening. Gusdorf et al. (2008a) found that the SiO intensity and line width as the shock dissipates. In Fig. 6, we plot the velocity dispersion of the four groups (Section 3) against dust temperature ($T_{\rm d}$), the particle number density (n) of the clumps, the SiO luminosity ($L_{\rm sio}$), and the bolometric luminosity to mass ratio ($L_{\rm bol}/M$) of clumps from Liu et al. (2020a), respectively. The particle number density can be derived as

$$n = \frac{3M_{gas}}{4\pi R^3 m_H \mu}, \quad (2)$$

M and R the clump mass and effective radii compiled in Liu et al. (2020a). n is the particle number density. $m_{\rm H}$ is the mass of a hydrogen atom. $\mu = 2.37$ is the mean molecular weight per 'free particle'. $T_{\rm d}$ and $L_{\rm bol}/M$ are potential evolutionary tracers for high-mass protostars and their natal clumps (Molinari et al. 2008; Elia et al. 2021). More evolved sources show higher $T_{\rm d}$ and $L_{\rm bol}/M$.

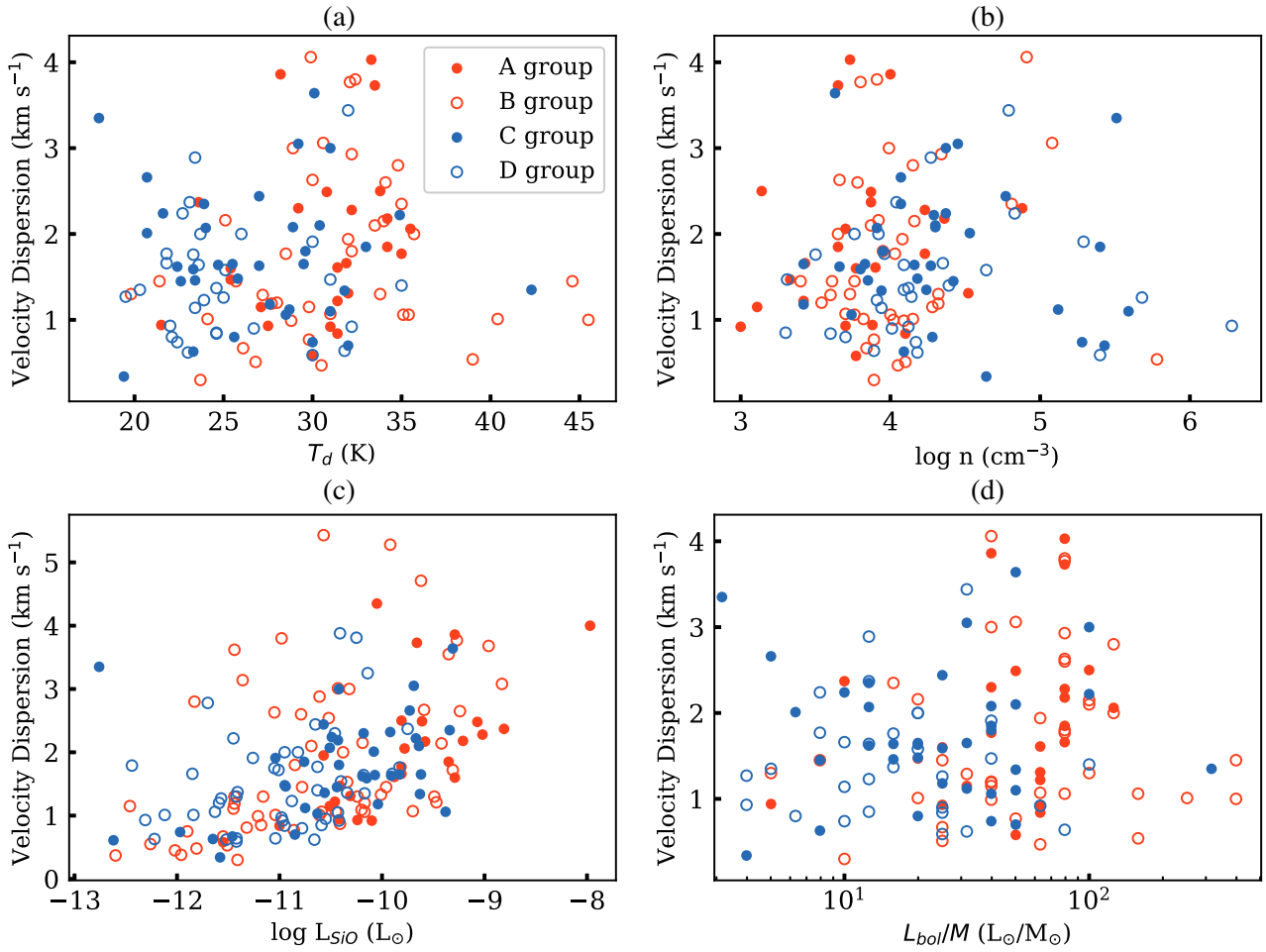

Figure 6. (a) The velocity dispersion of SiO emission against dust temperature ($T_{\rm d}$). (b) The velocity dispersion of SiO emission versus the particle number density (n) of the clumps. (c) The velocity dispersion of SiO emission against the SiO clump radius. (d) The velocity dispersion of SiO emission versus the bolometric luminosity to mass ratio ($L_{\rm bol}/M$). The filled red circles (A group) represent the SiO clumps containing HII regions are associated with 3 mm continuum emission. The empty red circles (B group) represent the SiO clumps containing HII regions are separated with 3 mm continuum emission. The filled blue circles (C group) represent the SiO clumps containing non-HII regions are associated with 3 mm continuum emission. The empty blue circles (D group) represent the SiO clumps containing non-HII regions are separated with 3 mm continuum emission.

As shown in Fig. 6, there is no obvious trend between the velocity dispersion of all groups SiO emission and either $T_{\rm d}$ or n. There is also no statistically significant correlation between the velocity dispersion of all groups and $L_{\rm bol}/M$. We use the Spearman-rank correlation test between those quantities, and the correlation coefficient is 0.15, 0.06, and 0.13, respectively. In our samples, we found no obvious variations in the velocity dispersion of the SiO emission against $T_{\rm d}$, n, and $L_{\rm bol}/M$, which indicates that the strengths of shocks are not so different under different physical conditions or at various evolutionary stages. Our results are consistent with the results of Csengeri et al. (2016) and Li et al. (2019a), who also found the line width of SiO emission is nearly constant at different evolutionary stages of clumps. In A, B, C groups, the $L_{\rm sio}$ has a positive correlation with the velocity dispersion of SiO emission, with a correlation coefficient of 0.72, 0.55, and 0.44, respectively. These results suggest that the more intense SiO sources are associated with more active outflows. Whereas in the D group, the $L_{\rm sio}$ does not correlate with the velocity dispersion of SiO emission. It means its presence of relatively strong SiO emission sources has smaller velocity dispersion. One would expect these SiO clumps may be due to the aging of outflows as it moves away from its driving source. An alternative explanation is to consider some of these SiO sources caused by unresolved lower mass protostars, cloud–cloud collision, or gas inflows. We will investigate these scenarios in the following work with high resolution 12-m array data.

4.2 The excitation condition for SiO emission

We examine the relationship between the bolometric luminosity and SiO emission-line luminosity in all groups. Fig. 7 shows the SiO line luminosity versus the bolometric luminosity in the upper panel. We exclude two low-mass star-forming sources (I08076-3556 and I11590-6452; Liu et al. 2020a). We can see an increasing trend between these two quantities in all groups. But in the A and B groups (with HII regions), the increasing trend is much steeper. Thus we get two linear fits. In the groups with HII regions, a linear fit is $f(x) = (1.06 \pm 0.12)x - 15.77$ and in the groups without HII regions, another linear fit is $f(x) = (0.54 \pm 0.11)x - 12.84$. The Spearman rank correlation coefficient (p) is 0.7 and 0.58, respectively. This implies that higher luminosity sources could have brighter SiO emission,

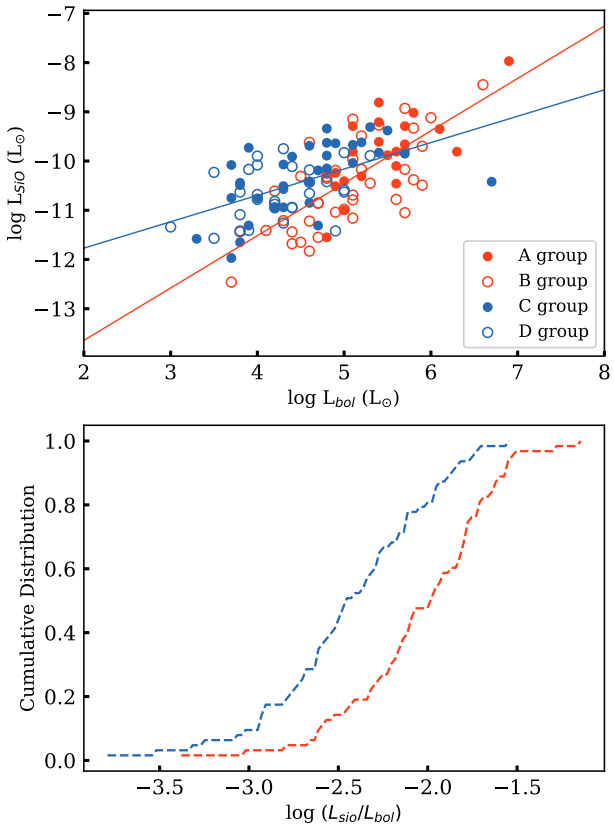

Figure 7. Upper panel: SiO (2-1) line luminosity $L_{\rm SiO}$ versus bolometric luminosity $L_{\rm bol}$. The red line shows a linear fit of $f(x) = (1.06 \pm 0.12)x - 15.77$ and the blue line a linear fit of $f(x) = (0.54 \pm 0.11)x - 12.84$. The symbols are the same with Fig. 6. Lower panel: The $L_{\rm SiO}/L_{\rm bol}$ distributions for SiO clumps with HII regions and without HII regions (the red and blue lines).

indicating stronger shock activity in more luminous proto-clusters. These results are consistent with the results of Codella et al. (1999) and Liu et al. (2021c), who both found a trend of brighter SiO emission in higher luminosity sources. As for the different slope of $L_{\rm sio}/L_{\rm bol}$, this could be due to the different evolutionary stages of these sources. Next, we plot the cumulative distribution of the $L_{\rm sio}/L_{\rm bol}$ for the SiO clumps with HII regions and without HII regions in the lower panel. The KS test reveals that the p-value is 10^{-5}, indicating the $L_{\rm sio}/L_{\rm bol}$ for these two groups is from different distributions. Sources containing HII regions show relatively lower $L_{\rm sio}/L_{\rm bol}$ ratios, indicating that HII regions may have negative feedback on surrounding gas and may suppress further star formation, leading to less energetic outflows and thus weaker shocks.

Fig. 8 shows [SiO]/[$H^{13}CO^+$] intensity ratio as a function of $T_{\rm d}$ and n in all groups (p $= -0.13$, 0.12, respectively). However, we find the fraction of shocked gas increase as the n increase in A group (p $= 0.5$). Summarizing, in a large fraction of sources (except for the A group), the fraction of shocked gas shows no essential dependence on the $T_{\rm d}$ and n. This indicates that SiO emission is not affected by thermal condition but is more likely affected by shock activities. However, $H^{13}CO^+$ abundance may not be constant with time (Sanhueza et al. 2012), which may affect the interpretation of [SiO]/[$H^{13}CO^+$] ratios.

The bolometric luminosity of a molecular clump will increase as the high mass star evolves, while its mass will decrease. Thus the bolometric luminosity to mass ratio ($L_{\rm bol}/M$) can be a good tracer of the evolutionary stage of star formation (Molinari et al. 2008, 2016; Elia et al. 2021). $L_{\rm bol}/M$ values can distinguish between the young and evolved sources, and its low values are related to young sources. In the left-hand panel of Fig. 9, we plot the SiO luminosity ($L_{\rm SiO}$) against $L_{\rm bol}/M$ in all groups (p $= 0.3$, -0.04, 0.32, and -0.12, respectively). The $L_{\rm SiO}$ does not vary with $L_{\rm bol}/M$, suggesting that SiO luminosity has no relationship with evolutionary stages, which is similar to the results of Liu et al. (2021c). The right-hand panel shows [SiO]/[$H^{13}CO^+$] versus $L_{\rm bol}/M$. There is also no correlation between [SiO]/[$H^{13}CO^+$] and $L_{\rm bol}/M$. This implies that the fraction of shocked gas in high-mass star-forming clumps does not change obviously in dense gas at various evolutionary stages. This is consistent with the results reported by Csengeri et al. (2016) and Li et al. (2019a).

5 SUMMARY

In this work, we used ALMA ACA observational data for a statistical study of shocked gas toward 146 massive star-forming regions. We analyse the variation of SiO emission under different physical conditions and evolutionary stages. The main results are summarized as follows:

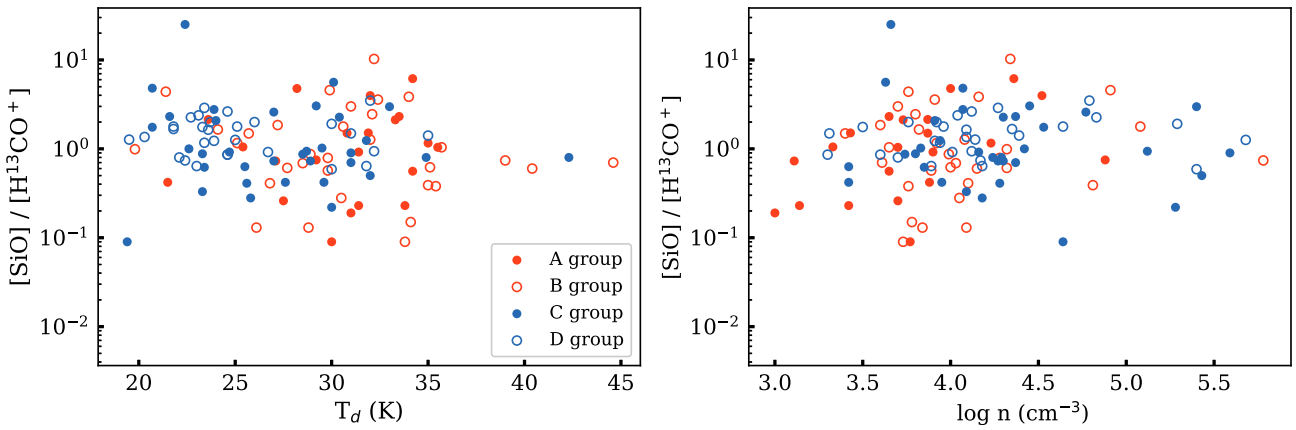

Figure 8. Left: [SiO]/[$H^{13}CO^+$] against dust temperature ($T_{\rm d}$). Right: [SiO]/[$H^{13}CO^+$] versus particle number density (n). The symbols are the same as in Fig. 6.

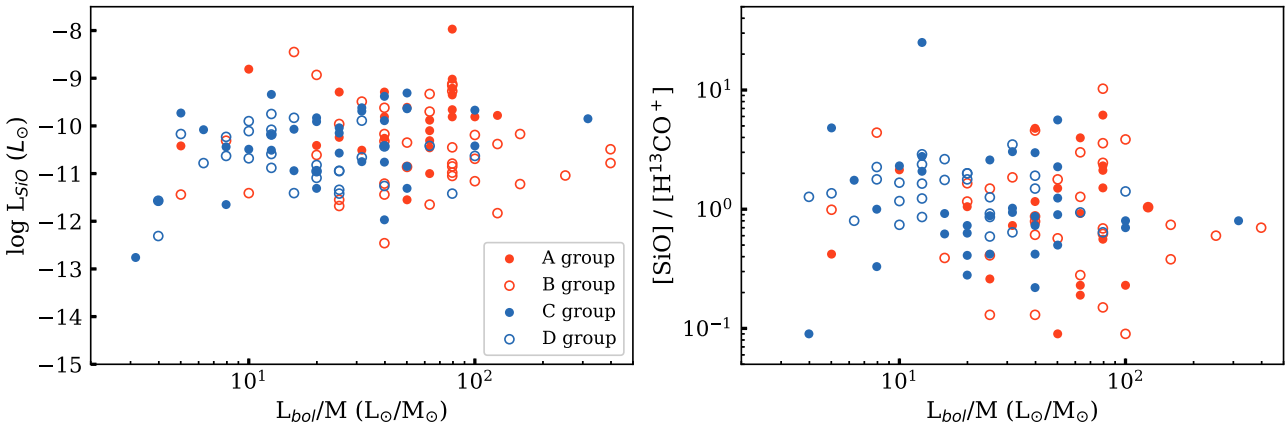

Figure 9. Left: The SiO line luminosity versus $L_{\rm bol}/M$ in the clumps. Right: [SiO]/[$H^{13}CO^+$] versus $L_{\rm bol}/M$. The symbols are the same with Fig. 6.

(1) Among the entire sample, we have detected SiO emission in 128 sources, which contain 171 SiO clumps. SiO (2-1) emission has a high detection rate of 87.7 per cent, above 3σ.

(2) The velocity dispersion of SiO line emission ranges from 0.3 to 5.43 km s^{-1}, with a median velocity dispersion of 1.59 km s^{-1}. Based on the high-velocity emission wings in SiO, HCO^+, and CS lines, we divided the clumps into two groups. There are 116 SiO clumps associated with strong outflows, which show high-velocity wing emission in at least one line, while the other 50 SiO clumps show no wing emission in the three lines and seem to be not associated with energetic outflows. The two groups have an obvious difference in the velocity dispersion of SiO emission. The median velocity dispersion of outflow sources is 1.91 km s^{-1}, which is significantly larger than that (0.99 km s^{-1}) of the non-outflow sources, indicating that outflow activities have a great influence on the strongly shocked gas. In particular, SiO emission clumps with small velocity dispersion could be formed by low-velocity shocks that are induced by either HII regions or other large-scale compression flows (e.g. cloud–cloud collision), which will be investigated thoroughly in forthcoming works with higher resolution ALMA 12-m array data.

(3) We find a positive correlation between the SiO line luminosity and the bolometric luminosity, implying stronger shock activities associated with more luminous proto-clusters. We also find the SiO clumps with HII regions show a lower $L_{\rm SiO}/L_{\rm bol}$ ratio than the SiO clumps without HII regions. In most sources, the velocity dispersion of SiO emission and [SiO]/[$H^{13}CO^+$] show no obvious correlations with dust temperature ($T_{\rm d}$) and particle number density (n). These results indicated that the SiO emission is not likely affected by thermal conditions but is more likely affected by shock activities. In addition, we do not see clear correlations between the SiO line luminosity and $L_{\rm bol}/M$. There is also no robust trend in the [SiO]/[$H^{13}CO^+$] and $L_{\rm bol}/M$ relation. This implies that the fraction of shocked gas in dense gas does not change obviously at various evolutionary stages.

ACKNOWLEDGEMENTS

TL acknowledges the supports by National Natural Science Foundation of China (NSFC) through grants No.12073061 and No.12122307, the international partnership program of Chinese academy of sciences through grant No.114231KYSB20200009, and Shanghai Pujiang Program 20PJ1415500. This work is supported by the Ministry of Science and Technology of China through grant 2010DFA02710, the Key Project of International Cooperation, and by the National Natural Science Foundation of China (NSFC) through grants 11503035, 11573036. HLL is supported by NSFC through the grant No.12103045. KW acknowledges support by the National Science Foundation of China (12041305, 11973013) and the High-Performance Computing Platform of Peking University through the instrumental analysis fund of Peking University (0000057511). This research was carried out in part at the Jet Propulsion Laboratory, which is operated by the California Institute of Technology under a contract with the National Aeronautics and Space Administration (80NM0018D0004). GG and LB acknowledge support by the ANID BASAL project FB210003. SL Qin is supported by NSFC under grant No. 12033005. CWL is supported by the Basic Science Research Program through the National Research Foundation of Korea (NRF) funded by the Ministry of Education, Science and Technology (NRF-2019R1A2C1010851). YZ acknowledges financial support from NSFC (grant No. 11973099). JHH thanks the National Natural Science Foundation of China under grant No. 11873086. This work is sponsored (in part) by the Chinese Academy of Sciences (CAS), through a grant to the CAS South America Center for Astronomy (CASSACA) in Santiago, Chile. GYZ acknowledges support by China Postdoctoral Science Foundation (No. 2021T140672). C.E. acknowledges the financial support from grant RJF/2020/000071 as a part of Ramanujan Fellowship awarded by Science and Engineering Research Board (SERB), Department of Science and Technology (DST), Govt. of India. This paper makes use of the following ALMA data: ADS/JAO.ALMA#2019.1.00685.S. ALMA is a partnership of ESO (representing its member states), NSF (USA), and NINS (Japan), together with NRC (Canada), MOST and ASIAA (Taiwan), and KASI (Republic of Korea), in cooperation with the Republic of Chile.

DATA AVAILABILITY

The data underlying this article are available in the article and in ALMA archive.

REFERENCES

Bally J., 2016, ARA&A, 54, 491
Bronfman L., Nyman L. A., May J., 1996, A&AS, 115, 81
Churchwell E. d., 2002, in The Formation and Early Evolution of Massive Stars, Hot Star Workshop III: The Earliest Phases of Massive Star Birth. Vol. 267, p. 3
Codella C., Bachiller R., Reipurth B., 1999, A&A, 343, 585

Cosentino G. et al., 2020, MNRAS, 499, 1666
Csengeri T. et al., 2016, A&A, 586, A149
Duarte-Cabral A., Bontemps S., Motte F., Gusdorf A., Csengeri T., Schneider N., Louvet F., 2014, A&A, 570, A1
Elia D. et al., 2021, MNRAS, 504, 2742
Gerner T., Beuther H., Semenov D., Linz H., Vasyunina T., Bihr S., Shirley Y. L., Henning T., 2014, A&A, 563, A97
Gusdorf A., Cabrit S., Flower D. R., Pineau Des Forêts G., 2008a, A&A, 482, 809
Gusdorf A., Pineau Des Forêts G., Cabrit S., Flower D. R., 2008b, A&A, 490, 695
Jiménez-Serra I., Caselli P., Tan J. C., Hernandez A. K., Fontani F., Butler M. J., van Loo S., 2010, MNRAS, 406, 187
Lefloch B., Castets A., Cernicharo J., Loinard L., 1998, ApJ, 504, L109
Leurini S., Codella C., López-Sepulcre A., Gusdorf A., Csengeri T., Anderl S., 2014, A&A, 570, A49
Li S. et al., 2019a, ApJ, 878, 29
Li S. et al., 2020, ApJ, 903, 119
Li S., Zhang Q., Pillai T., Stephens I. W., Wang J., Li F., 2019b, ApJ, 886, 130
Liu T. et al., 2020a, MNRAS, 496, 2790
Liu T. et al., 2020b, MNRAS, 496, 2821
Liu M., Tan J. C., Marvil J., Kong S., Rosero V., Caselli P., Cosentino G., 2021c, ApJ, 921, 96
Liu H.-L. et al., 2021a, MNRAS, 510, 5009
Liu H.-L. et al., 2021b, MNRAS, 505, 0035
Liu H.-L., Sanhueza P., Liu T., Zavagno A., Tang X.-D., Wu Y., Zhang S., 2020c, ApJ, 901, 31
López-Sepulcre A. et al., 2011, A&A, 526, L2
López-Sepulcre A., Watanabe Y., Sakai N., Furuya R., Saruwatari O., Yamamoto S., 2016, ApJ, 822, 85
Louvet F. et al., 2016, A&A, 595, A122
Martin-Pintado J., Bachiller R., Fuente A., 1992, A&A, 254, 315
McMullin J. P., Waters B., Schiebel D., Young W., Golap K., 2007, in Shaw R. A., Hill F., Bell D. J., eds, ASP Conf. Ser. Vol. 376, Astronomical Data Analysis Software and Systems XVI. Astron. Soc. Pac., San Francisco, p. 127
Miettinen O., 2014, A&A, 562, A3
Miettinen O., Harju J., Haikala L. K., Pomrén C., 2006, A&A, 460, 721
Molinari S., Pezzuto S., Cesaroni R., Brand J., Faustini F., Testi L., 2008, A&A, 481, 345
Molinari S., Merello M., Elia D., Cesaroni R., Testi L., Robitaille T., 2016, ApJ, 826, L8
Motte F., Bontemps S., Schilke P., Schneider N., Menten K. M., Broguière D., 2007, A&A, 476, 1243
Motte F., Bontemps S., Louvet F., 2018, ARA&A, 56, 41
Myers P. C., Mardones D., Tafalla M., Williams J. P., Wilner D. J., 1996, ApJ, 465, L133
Nomura H., Millar T. J., 2004, A&A, 414, 409
Qiu K., Zhang Q., Beuther H., Yang J., 2007, ApJ, 654, 361
Sakai T., Sakai N., Hirota T., Yamamoto S., 2010, ApJ, 714, 1658
Sánchez-Monge A., López-Sepulcre A., Cesaroni R., Walmsley C. M., Codella C., Beltrán M. T., Pestalozzi M., Molinari S., 2013, A&A, 557, A94
Sanhueza P., Jackson J. M., Foster J. B., Garay G., Silva A., Finn S. C., 2012, ApJ, 756, 60
Schilke P., Walmsley C. M., Pineau des Forets G., Flower D. R., 1997, A&A, 321, 293
Zinnecker H., Yorke H. W., 2007, ARA&A, 45, 481

SUPPORTING INFORMATION

Supplementary data are available at *MNRAS* online.

Figure A1. All detected sources. Left: The background is SiO (2-1) integrated intensity maps.

Please note: Oxford University Press is not responsible for the content or functionality of any supporting materials supplied by the authors. Any queries (other than missing material) should be directed to the corresponding author for the article.

APPENDIX A:

Fig. A1 present the moment maps and spectra for some exemplar sources. The images for all sources are available as on-line supplementary material. Tables A1, A2, and A3 show the derived parameters for SiO clumps.

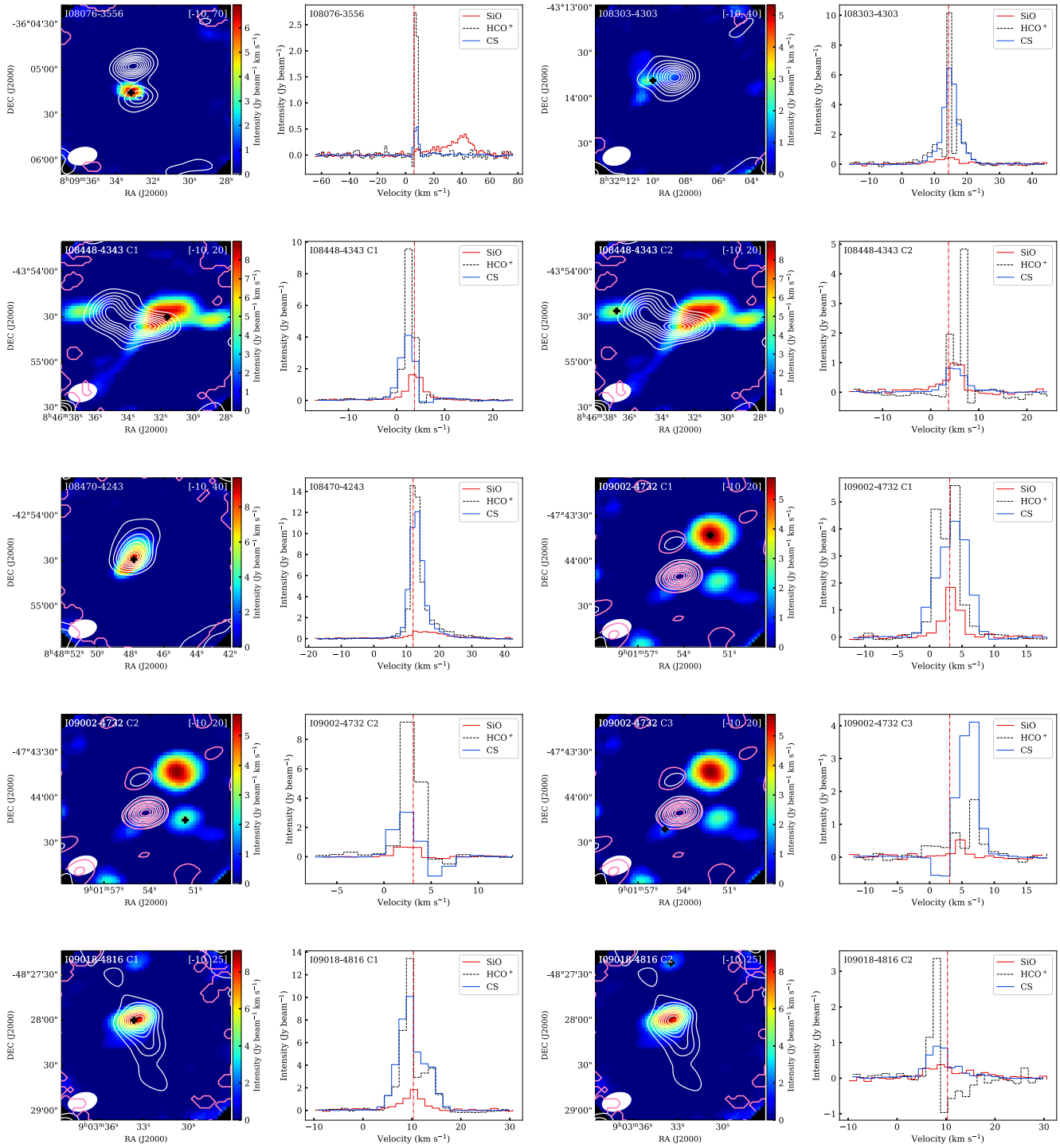

Figure A1. Examples of sources. Left: The background is SiO (2-1) integrated intensity maps. The white contours are 3mm continuum emission, and contours are from 10 per cent to 100 per cent in the step of 10 per cent of peak values. The pink contours represent H40α emission, and contours are from 10 per cent to 100 per cent in the step of 20 per cent of peak values. The black cross is the position extracted spectra. The source name is shown on the upper left. The integration velocity ranges are shown in the upper right corner. Right: The clump averaged SiO, HCO^+ and CS spectra are shown in red, black dashed, and blue lines, respectively. The vertical dash–dotted line indicates the systemic velocity of the source. The full images are available as supplementary material.

Table A1. SiO (2-1) line parameters and clump properties in the region with clear detections.

IRAS	RA (J2000)	DEC (J2000)	R_a (pc)	$\int F_\nu d\nu$ (Jy km s^{-1})	v (km s^{-1})	σ_v (km s^{-1})				log L_{SiO} ($L_\odot$)	σ (Jy beam^{-1})
						D_{min}	D_{max}	D_{mean}	D_{median}	D_{std}	
I08076-3556	08:09:33.21	−36:05:14.2	0.03[a]	3.47 ± 0.26	39.4 ± 2.47	0.96	8.6	3.71	3.35	3.26	− 12.76 ± 0.031	0.099
I08303-4303	08:32:10.05	−43:13:47.71	0.05 ± 0.066	2.3 ± 0.61	14.61 ± 0.23	0.17	1.69	0.67	0.59	0.17	− 11.42 ± 0.102	0.123
I08448-4343 C1	08:46:31.64	−43:54:29.1	0.07 ± 0.016	24.7 ± 4.5	3.6 ± 1.94	0.35	2.6	1.29	1.3	0.29	− 11.42 ± 0.073	0.124
C2	08:46:36.78	−43:54:26.2	0.05[a]	4.96 ± 0.36	4.11 ± 0.92	0.32	2.07	1.08	1.01	0.22	− 12.12 ± 0.03	0.124
I08470-4243	08:48:47.86	−42:54:28.9	0.15[a]	12.4 ± 1.2	14.66 ± 4.17	0.32	5.16	2.21	1.85	1.65	− 10.76 ± 0.04	0.121
I09002-4732 C1	09:01:52.18	−47:43:42.7	0.06 ± 0.019	10.46 ± 0.84	2.78 ± 0.08	0.29	1.27	0.8	0.81	0.05	− 11.32 ± 0.034	0.128
C2	09:01:51.71	−47:44:14.1	0.09[a]	2.41 ± 0.3	1.86 ± 0.02	0.17	0.56	0.38	0.38	0.01	− 11.96 ± 0.051	0.128
C3	09:01:55.28	−47:44:21.7	0.09[a]	0.55 ± 0.05	4.08 ± 0.06	0.17	0.59	0.36	0.37	0.02	− 12.6 ± 0.038	0.128
I09018-4816 C1	09:03:33.61	−48:27:59.3	0.09 ± 0.047	11.11 ± 0.9	9.64 ± 0.31	0.3	1.9	1.04	1.03	0.21	− 10.63 ± 0.034	0.115
C2	09:03:33.4	−48:27:21.6	0.19[a]	1.21 ± 0.16	7.92 ± 0.95	0.39	5.24	1.49	1.2	0.71	− 11.59 ± 0.054	0.115
I09094-4803	09:11:08.42	−48:15:43.0	0.71[a]	0.76 ± 0.07	74.19 ± 0.04	0.17	0.8	0.54	0.62	0.04	− 10.66 ± 0.038	0.128
I10365-5803	10:38:33.17	−58:19:14.4	0.19[a]	3.02 ± 0.34	− 22.24 ± 6.94	0.36	2.53	1.73	1.91	0.38	− 11.26 ± 0.046	0.093
I11298-6155	11:32:05.36	−62:12:26.3	0.78[a]	1.55 ± 0.1	33.13 ± 0.32	0.72	1.87	1.36	1.31	0.14	− 10.31 ± 0.027	0.124
I11332-6258	11:35:32.00	−63:14:45.1	0.15[a]	0.95 ± 0.04	− 15.68 ± 0.43	0.17	1.16	0.79	0.74	0.04	− 11.97 ± 0.018	0.125
I11590-6452	12:01:39.09	−65:09:03.7	0.03[a]	9.82 ± 0.96	1.68 ± 0.36	0.17	2.37	0.87	0.93	0.12	− 12.31 ± 0.041	0.123
I12320-6122	12:34:52.43	−61:39:52.0	0.14	4.48 ± 0.71	− 43.35 ± 1.25	0.29	3.32	1.42	1.45	0.58	− 10.78 ± 0.064	0.130
I12326-6245	12:35:34.85	−63:02:29.4	0.23 ± 0.039	92.9 ± 4.5	− 39.9 ± 2.41	0.53	6.8	2.5	2.18	2.35	− 9.21 ± 0.021	0.123
I12572-6316	13:00:24.41	−63:32:31.8	0.91[a]	0.91 ± 0.01	29.85 ± 0.21	0.17	1.18	0.82	0.94	0.09	− 10.42 ± 0.005	0.131
I13079-6218	13:11:14.11	−62:34:45.4	0.12 ± 0.026	114.3 ± 3	− 40.24 ± 1.13	0.75	7.14	3.86	3.86	3.59	− 9.29 ± 0.011	0.138
I13111-6228	13:14:26.50	−62:44:26.9	0.3[a]	0.62 ± 0.06	− 38.83 ± 0.48	0.32	0.93	0.59	0.58	0.02	− 11.55 ± 0.04	0.123
I13134-6242	13:16:43.88	−62:58:32.5	0.3[a]	45 ± 2.3	− 31.78 ± 2.66	0.59	5.2	2.97	3.05	1.78	− 9.69 ± 0.022	0.125
I13140-6226	13:17:15.68	−62:42:27.1	0.3[a]	7.94 ± 0.56	− 34.56 ± 0.65	0.17	2.86	1.48	1.45	0.6	− 10.44 ± 0.03	0.138
I13291-6249	13:32:32.05	−63:05:08.3	0.61[a]	17.7 ± 2.9	− 32.62 ± 2.78	0.29	7.84	2.16	1.3	3.14	− 9.49 ± 0.066	0.137
I13295-6152	13:32:52.90	−62:07:49.2	0.31[a]	0.55 ± 0.06	− 45.08 ± 0.03	0.17	0.45	0.32	0.34	0.0	− 11.58 ± 0.045	0.129
I13471-6120	13:50:44.03	−61:35:07.5	0.44[a]	3.82 ± 0.47	− 59.11 ± 1.01	0.23	2.22	1.15	1.06	0.31	− 10.45 ± 0.05	0.119
I13484-6100	13:51:58.44	−61:15:36.5	0.24 ± 0.086	25.6 ± 2.6	− 54.99 ± 0.26	0.47	4.14	1.52	1.34	0.62	− 9.63 ± 0.042	0.127
I14013-6105	14:04:54.67	−61:20:07.6	0.33[a]	1.88 ± 0.19	− 55.31 ± 0.11	0.42	1.0	0.81	0.84	0.03	− 11 ± 0.042	0.126
I14164-6028	14:20:08.47	−60:42:01.6	0.26 [a]	5.58 ± 0.27	− 46.94 ± 0.05	0.35	2.01	1.15	1.12	0.23	− 10.75 ± 0.021	0.120
I14212-6131	14:25:04.65	−61:44:55.8	0.24 ± 0.045	33.7 ± 3.1	− 49.99 ± 1.08	0.49	2.96	1.72	1.66	0.44	− 9.9 ± 0.038	0.127
I14453-5912	14:49:06.37	−59:24:36.3	0.13	9.8 ± 1.4	− 40.79 ± 0.26	0.23	1.58	0.94	1.01	0.12	− 10.61 ± 0.058	0.148
I14498-5856 C1	14:53:43.74	−59:08:54.0	0.23[a]	2.88 ± 0.34	− 50.6 ± 0.12	0.21	1.37	0.79	0.64	0.15	− 11.04 ± 0.048	0.141
C2	14:53:44.58	−59:09:29.6	0.23[a]	0.75 ± 0.04	− 51.97 ± 0.66	0.22	1.79	1.11	1.06	0.26	− 11.63 ± 0.023	0.141
I15290-5546	15:32:52.77	−55:56:04.3	0.47[a]	15.36 ± 0.97	− 85.76 ± 2.44	0.23	6.24	3.73	3.73	3.21	− 9.66 ± 0.027	0.148
I15394-5358	15:43:16.66	−54:07:14.7	0.2 ± 0.023	80.5 ± 6.3	− 41.15 ± 8.28	0.41	3.51	1.96	2.01	0.71	− 10.08 ± 0.033	0.158
I15408-5356	15:44:43.32	−54:05:20.8	0.2 ± 0.037	62.5 ± 7.9	− 36.54 ± 1.28	0.55	4.54	2.27	2.15	0.82	− 10.19 ± 0.052	0.149
I15411-5352 C1	15:44:59.27	−54:02:25.5	0.13[a]	1.22 ± 0.1	− 43.09 ± 0.05	0.21	1.77	0.79	0.75	0.14	− 11.9 ± 0.034	0.148
C2	15:45:00.13	−54:01:39.4	0.13[a]	0.91 ± 0.12	− 43.25 ± 2.08	0.17	1.76	0.48	0.45	0.07	− 12.02 ± 0.054	0.148
I15439-5449 C1	15:47:46.18	−54:58:16.6	0.24[a]	0.46 ± 0.05	− 55.71 ± 0.45	0.32	0.9	0.54	0.48	0.02	− 11.81 ± 0.045	0.148
C2	15:47:48.78	−54:58:10.2	0.24[a]	0.16 ± 0.08	− 54.44 ± 0.14	0.3	0.92	0.55	0.55	0.03	− 12.26 ± 0.176	0.148
I15520-5234 C1	15:55:50.17	−52:43:13.8	0.24 ± 0.027	202 ± 16	− 41.66 ± 2.55	0.58	5.73	3.26	3.55	1.52	− 9.35 ± 0.033	0.156
C2	15:55:48.04	−52:43:09.4	0.2 ± 0.042	118 ± 11	− 45.68 ± 0.66	0.91	2.85	2.1	2.17	0.27	− 9.58 ± 0.039	0.156
I15522-5411	15:56:07.13	−54:20:02.6	0.2[a]	0.95 ± 0.1	− 47.44 ± 0.07	0.3	1.17	0.66	0.63	0.06	− 11.65 ± 0.043	0.157
I15557-5215	15:59:40.96	−52:23:27.6	0.3[a]	36.8 ± 2.6	− 68.02 ± 13.86	0.3	6.58	2.74	2.66	2.23	− 9.73 ± 0.03	0.149
I15567-5236	16:00:33.56	−52:44:39.1	0.44[a]	5.98 ± 0.74	− 107.71 ± 1.59	0.17	5.39	1.75	1.06	2.44	− 10.17 ± 0.051	0.155
I15584-5247	16:02:20.54	- 52:55:13.0	0.32[a]	2.15 ± 0.16	− 77.13 ± 1.35	0.3	2.22	1.08	1.23	0.24	− 10.88 ± 0.031	0.158
I15596-5301	16:03:32.55	−53:09:29.8	0.74[a]	13.1 ± 1.2	− 73.1 ± 0.88	0.3	1.66	1.04	1.06	0.11	− 9.38 ± 0.038	0.159
I16026-5035	16:06:24.78	- 50:43:06.2	0.33[a]	0.59 ± 0.03	− 79.97 ± 0.05	0.24	0.82	0.61	0.64	0.03	− 11.42 ± 0.022	0.166
I16037-5223	16:07:38.08	−52:31:00.9	0.72[a]	1.152 ± 0.07	− 80.1 ± 0.91	0.41	1.76	1.17	1.22	0.16	− 10.46 ± 0.026	0.156
I16060-5146	16:09:52.40	−51:54:56.2	0.49 ± 0.067	109 ± 8.9	− 90.96 ± 3.62	0.61	4.37	2.37	2.28	1.18	− 9.02 ± 0.034	0.160
I16065-5158	16:10:20.09	−52:06:11.0	0.14	49.6 ± 3	− 64.04 ± 0.5	0.46	5.72	2.67	2.49	1.67	− 9.61 ± 0.026	0.155
I16071-5142	16:10:59.84	−51:50:21.2	0.18 ± 0.031	51.4 ± 1.7	− 86.48 ± 0.47	0.3	5.01	2.56	2.35	1.66	− 9.34 ± 0.014	0.153
I16076-5134	16:11:26.66	−51:41:56.3	0.39[a]	56.1 ± 1.6	− 86.74 ± 0.41	0.69	6.67	3.66	3.64	2.98	− 9.31 ± 0.012	0.158
I16119-5048	16:15:45.35	−50:55:52.5	0.23[a]	10.17 ± 0.58	− 51.19 ± 0.54	0.55	4.18	2.32	2.07	0.89	− 10.51 ± 0.024	0.158
I16164-5046	16:20:11.30	- 50:53:16.7	0.09	33.2 ± 1.9	− 55.12 ± 1.21	0.48	3.3	1.72	1.61	0.56	− 9.88 ± 0.024	0.164
I16172-5028 C1	16:21:02.64	−50:35:00.4	0.25 ± 0.065	95.6 ± 9.7	− 52.32 ± 9.85	0.72	4.68	2.6	2.14	1.74	− 9.42 ± 0.042	0.159
C2	16:21:03.14	−50:35:49.6	0.26[a]	14.3 ± 1.9	− 49.82 ± 31.3	0.36	8.79	1.47	1.3	0.98	− 10.24 ± 0.054	0.159
C3	16:20:59.42	−50:35:53.1	0.26[a]	6.78 ± 0.94	− 50.55 ± 82.11	0.76	22.34	6.1	5.43	22.08	− 10.57 ± 0.056	0.159
I16272-4837	16:30:58.27	−48:43:45.2	0.32 ± 0.056	66.6 ± 8.7	− 46.32 ± 7.23	0.53	5.95	2.48	2.37	1.54	− 9.75 ± 0.053	0.163
I16297-4757	16:33:29.23	−48:03:45.6	0.36[a]	3.85 ± 0.26	− 80.13 ± 0.06	0.43	1.84	1.16	1.15	0.16	− 10.51 ± 0.028	0.168
I16318-4724	16:35:33.72	−47:31:10.1	0.54[a]	12.9 ± 0.64	− 121.48 ± 0.41	0.43	2.98	1.68	1.65	0.48	− 9.62 ± 0.021	0.174
I16344-4658	16:38:09.36	−47:04:59.4	0.86[a]	3.23 ± 0.16	− 49.88 ± 0.6	0.64	2.25	1.57	1.65	0.2	− 9.83 ± 0.021	0.172
I16348-4654	16:38:29.27	−47:00:39.0	0.86[a]	33.7 ± 3.5	− 47.53 ± 2.12	0.45	3.6	2.27	2.37	0.6	− 8.81 ± 0.043	0.157
I16351-4722	16:38:50.40	−47:27:58.3	0.18 ± 0.069	79.4 ± 8	− 40.4 ± 4.29	0.23	6.61	2.42	2.1	2.46	− 9.64 ± 0.042	0.177
I16385-4619	16:42:13.74	−46:25:29.8	0.51[a]	9.84 ± 0.59	− 119.57 ± 0.64	0.53	2.96	1.76	1.66	0.49	− 9.81 ± 0.025	0.176
I16424-4531	16:46:06.26	−45:36:39.0	0.18[a]	1.78 ± 0.14	− 31.75 ± 30.16	0.17	6.37	2.6	1.37	5.17	− 11.41 ± 0.033	0.173
I16445-4459	16:48:04.54	−45:05:03.9	0.55[a]	1.3 ± 0.08	− 121.08 ± 0.23	0.24	1.09	0.8	0.85	0.05	− 10.59 ± 0.026	0.164
I16458-4512 C1	16:49:29.22	−45:18:09.3	0.25[a]	11.4 ± 1.8	− 50.77 ± 1.97	0.36	4.93	1.63	1.53	0.89	− 10.34 ± 0.064	0.167
C2	16:49:32.31	−45:17:30.0	0.25[a]	0.78 ± 0.08	− 49.19 ± 0.15	0.24	1.88	0.56	0.53	0.07	− 11.51 ± 0.042	0.167
I16484-4603	16:52:02.10	−46:08:16.6	0.15[a]	17.1 ± 1.5	− 33.15 ± 1.62	0.65	3.53	1.57	1.4	0.48	− 10.63 ± 0.037	0.165
I16487-4423	16:52:23.92	−44:27:47.9	0.23[a]	3.36 ± 0.3	− 42.69 ± 0.23	0.17	1.22	0.74	0.84	0.1	− 10.95 ± 0.037	0.169
I16489-4431	16:52:34.13	−44:36:26.0	0.22[a]	6.98 ± 0.6	− 40.45 ± 1.61	0.3	2.67	1.69	1.77	0.35	− 10.63 ± 0.036	0.162

Table A1 – *continued*

IRAS	RA (J2000)	DEC (J2000)	R_a (pc)	$\int F_\nu dv$ (Jy km s^{-1})	v (km s^{-1})	σ_v (km s^{-1})					log L_{SiO} ($L_\odot$)	σ (Jy beam^{-1})
						D_{min}	D_{max}	D_{mean}	D_{median}	D_{std}		
I16524-4300 C1	16:56:03.80	−43:04:59.7	0.24 ± 0.083	12.4 ± 2.2	−41.45 ± 1.8	0.35	2.17	1.24	1.36	0.22	−10.34 ± 0.071	0.106
C2	16:56:02.36	−43:04:18.9	0.15 ± 0.089	7.7 ± 1.2	−40.73 ± 2.38	0.17	2.33	1.09	0.95	0.38	−10.55 ± 0.063	0.106
C3	16:56:06.55	−43:04:12.5	0.25[a]	0.81 ± 0.1	−42.1 ± 0.2	0.23	1.09	0.63	0.62	0.05	−11.52 ± 0.051	0.106
I16547-4247 C1	16:58:16.79	−42:52:03.0	0.17 ± 0.057	50.7 ± 5.2	−29.37 ± 1.77	0.51	4.58	2.26	2.32	1.25	−9.92 ± 0.042	0.119
C2	16:58:18.11	−42:52:37.2	0.2[a]	3.81 ± 0.92	−36.64 ± 2.34	0.57	5.02	2.12	1.75	0.95	−11.05 ± 0.094	0.119
I16562-3959 C1	16:59:41.33	−40:03:37.6	0.14	36.8 ± 3.9	−11.74 ± 5.39	0.46	4.95	2.36	2.3	1.65	−10.18 ± 0.044	0.115
C2	16:59:38.93	−40:04:11.0	0.1 ± 0.033	20.9 ± 1.6	−11.4 ± 0.44	0.3	1.53	1.01	1.05	0.11	−10.43 ± 0.032	0.115
C3	16:59:43.59	−40:03:08.5	0.16	22.2 ± 3	−10.53 ± 2.6	0.37	2.55	1.44	1.54	0.26	−10.4 ± 0.055	0.115
I16571-4029	17:00:32.34	−40:34:08.0	0.17[a]	15.2 ± 0.68	−13.78 ± 1.32	0.48	4.71	2.55	2.44	1.22	−10.57 ± 0.019	0.112
I17006-4215	17:04:11.88	−42:19:50.0	0.16[a]	2.39 ± 0.22	−21.78 ± 0.2	0.23	2.23	1.21	1.19	0.35	−11.44 ± 0.038	0.117
I17008-4040 C1	17:04:22.96	−40:44:19.6	0.16 ± 0.056	15.6 ± 2.8	−18.15 ± 2.77	0.23	2.54	1.35	1.36	0.4	−10.56 ± 0.072	0.120
C2	17:04:25.22	−40:44:28.4	0.17[a]	5.44 ± 0.74	−12.02 ± 5.12	0.68	2.82	1.72	1.72	0.35	−11.01 ± 0.055	0.120
I17016-4124 C1	17:05:10.61	−41:29:18.9	0.14 ± 0.037	122 ± 18	−26.25 ± 33.11	0.65	6.52	3.5	3.25	2.81	−10.14 ± 0.06	0.116
C2	17:05:11.25	−41:28:52.7	0.09	96.1 ± 9.2	−31.02 ± 14.83	0.63	7.13	3.97	3.81	3.41	−10.25 ± 0.04	0.116
I17143-3700	17:17:45.50	−37:03:12.5	0.87[a]	1.58 ± 0.13	−31.18 ± 0.24	0.36	1.38	0.87	0.92	0.04	−10.1 ± 0.034	0.140
I17158-3901	17:19:20.41	−39:03:49.5	0.12 ± 0.062	19.7 ± 2.1	−17.54 ± 2.0	0.34	3.11	1.65	1.59	0.6	−10.15 ± 0.044	0.159
I17160-3707 C1	17:19:26.61	−37:10:21.4	0.66	14 ± 1.9	−69.0 ± 7.56	0.42	2.89	1.69	1.72	0.42	−9.31 ± 0.055	0.151
C2	17:19:25.83	−37:10:02.8	0.72[a]	6.9 ± 1.4	−69.92 ± 26.24	0.62	18.32	6.3	4.71	25.68	−9.62 ± 0.08	0.151
C3	17:19:26.60	−37:11:12.6	0.72[a]	1.11 ± 0.09	−69.17 ± 0.21	0.35	1.38	0.88	0.87	0.13	−10.41 ± 0.034	0.151
I17175-3544 C1	17:20:52.71	−35:47:04.9	0.09[a]	65.5 ± 9.8	−9.18 ± 13.26	0.35	9.7	3.8	3.01	9.74	−10.43 ± 0.061	0.155
C2	17:20:54.55	−35:46:46.8	0.09[a]	7.7 ± 2.1	1.17 ± 0.5	0.91	4.44	2.93	3.14	1.17	−11.36 ± 0.105	0.155
C3	17:20:50.26	−35:46:40.7	0.09[a]	6.48 ± 0.42	0.88 ± 10.1	0.84	6.37	3.71	3.62	1.58	−11.44 ± 0.027	0.155
I17204-3636	17:23:50.18	−36:38:56.7	0.23[a]	3.21 ± 0.29	−19.79 ± 0.68	0.36	2.23	1.29	1.48	0.24	−10.95 ± 0.038	0.132
I17220-3609	17:25:25.09	−36:12:40.6	0.48 ± 0.222	25.6 ± 3.4	−94.88 ± 2.66	0.46	3.94	1.72	1.6	0.74	−9.29 ± 0.054	0.154
I17233-3606 C1	17:26:40.91	−36:09:26.8	0.14 ± 0.008	213.8 ± 9.6	1.68 ± 0.65	0.31	8.77	4.75	5.28	3.71	−9.92 ± 0.019	0.169
C2	17:26:42.53	−36:09:17.3	0.07	159 ± 19	2.47 ± 0.51	0.83	10.5	4.77	4.35	7.03	−10.05 ± 0.049	0.169
C3	17:26:45.55	−36:09:20.4	0.15 ± 0.031	53.3 ± 8.9	0.99 ± 0.51	0.67	5.03	2.83	2.54	1.81	−10.52 ± 0.067	0.169
I17244-3536	17:27:50.28	−35:38:57.8	0.09[a]	0.59 ± 0.04	−10.43 ± 0.28	0.46	1.44	1.15	1.15	0.04	−12.46 ± 0.028	0.148
I17258-3637 C1	17:29:18.35	−36:40:27.8	0.15 ± 0.051	12.1 ± 1.6	−13.37 ± 2.06	0.36	1.86	1.1	1.06	0.16	−10.59 ± 0.054	0.161
C2	17:29:18.65	−36:40:50.0	0.18[a]	3.13 ± 0.49	−10.86 ± 5.07	0.26	1.45	0.89	0.85	0.09	−11.18 ± 0.063	0.161
I17269-3312	17:30:14.47	−33:15:01.1	0.3[a]	10.73 ± 0.69	−24.11 ± 2.5	0.35	3.08	1.59	1.62	0.64	−10.19 ± 0.027	0.149
I17271-3439	17:30:26.8	−34:41:48.9	0.37 ± 0.091	51.6 ± 8	4.81 ± 0.0	0.24	3.71	1.66	1.77	0.72	−9.81 ± 0.063	0.148
I17278-3541 C1	17:31:15.88	−35:44:15.3	0.09[a]	6.45 ± 0.46	4.54 ± 2.61	0.37	3.29	1.97	2.22	0.84	−11.45 ± 0.03	0.151
C2	17:31:13.08	−35:43:41.8	0.09[a]	3.55 ± 0.17	−8.39 ± 4.01	0.58	4.03	2.57	2.78	1.14	−11.7 ± 0.02	0.151
C3	17:31:16.02	−35:43:27.2	0.09[a]	1.08 ± 0.12	0.94 ± 0.25	0.17	6.92	0.99	0.63	1.32	−12.22 ± 0.046	0.151
C4	17:31:16.52	−35:43:46.0	0.09[a]	2.54 ± 0.49	9.51 ± 27.86	0.57	4.06	2.03	1.66	0.75	−11.85 ± 0.077	0.151
C5	17:31:13.26	−35:44:07.9	0.09[a]	0.66 ± 0.03	−8.82 ± 0.74	0.35	2.19	1.58	1.79	0.32	−12.44 ± 0.019	0.151
C6	17:31:14.42	−35:43:58.0	0.09[a]	0.43 ± 0.05	0.44 ± 0.03	0.17	0.81	0.51	0.61	0.05	−12.62 ± 0.048	0.151
I17439-2845	17:47:10.18	−28:45:44.2	0.53[a]	0.44 ± 0.01	22.74 ± 1.63	0.74	3.6	2.29	2.63	0.73	−11.05 ± 0.01	0.105
I17441-2822 C1	17:47:22.78	−28:23:15.1	0.54[a]	71 ± 14	60.87 ± 22.29	0.45	9.32	3.82	3.08	8.19	−8.83 ± 0.078	0.526
C2	17:47:18.57	−28:23:15.8	0.54[a]	53 ± 11	58.9 ± 50.44	0.48	10.36	4.02	3.68	9.57	−8.96 ± 0.082	0.526
C3	17:47:22.06	−28:22:49.4	0.54[a]	28.1 ± 4.9	64.93 ± 40.02	0.74	5.85	3.16	2.65	2.7	−9.24 ± 0.07	0.526
C4	17:47:18.30	−28:22:46.6	0.54[a]	16.3 ± 3.4	59.47 ± 14.94	0.42	4.28	1.62	1.21	1.07	−9.47 ± 0.082	0.526
C5	17:47:20.82	−28:22:59.5	0.54[a]	4.75 ± 0.69	45.77 ± 0.4	0.54	2.07	1.33	1.33	0.18	−10.01 ± 0.059	0.526
I17455-2800	17:48:41.59	−28:01:56.2	0.67[a]	6.33 ± 0.53	−15.74 ± 0.48	0.24	2.02	1.11	1.07	0.27	−9.7 ± 0.035	0.129
I17545-2357	17:57:34.59	−23:57:32.5	0.2[a]	1.43 ± 0.38	7.56 ± 0.3	0.17	1.28	0.42	0.3	0.05	−11.41 ± 0.102	0.100
I17589-2312 C1	18:01:59.12	−23:12:56.7	0.21[a]	3.83 ± 0.65	23.84 ± 3.49	0.32	1.96	1.03	0.92	0.15	−10.97 ± 0.068	0.098
C2	18:01:58.39	−23:12:21.1	0.21[a]	3.78 ± 0.45	19.88 ± 1.68	0.35	2.31	1.01	0.97	0.23	−10.98 ± 0.049	0.098
I18032-2032	18:06:15.05	−20:31:37.7	0.18	64.8 ± 3.1	5.08 ± 5.54	0.38	10.76	4.26	3.77	8.97	−9.27 ± 0.02	0.088
I18056-1952 C1	18:08:38.16	−19:51:50.1	0.21	36.9 ± 1.7	66.88 ± 0.82	0.54	4.08	2.45	2.48	0.96	−9.07 ± 0.02	0.099
C2	18:08:38.00	−19:51:12.5	0.6[a]	11.32 ± 0.56	65.47 ± 5.17	0.3	4.86	2.5	2.67	1.95	−9.59 ± 0.021	0.099
C3	18:08:36.37	−19:52:14.3	0.6[a]	2.75 ± 0.2	70.98 ± 4.31	0.37	1.51	1.08	1.09	0.09	−10.2 ± 0.03	0.099
I18079-1756 C1	18:10:51.58	−17:55:46.5	0.13[a]	3.31 ± 0.43	18.02 ± 1.27	0.17	1.09	0.63	0.67	0.08	−11.46 ± 0.053	0.139
C2	18:10:49.38	−17:56:01.7	0.13[a]	1.37 ± 0.1	11.65 ± 0.35	0.29	1.43	0.93	1.01	0.06	−11.84 ± 0.031	0.139
I18089-1732	18:11:51.58	−17:31:25.6	0.18[a]	5.83 ± 0.28	33.25 ± 0.97	0.3	2.74	1.54	1.46	0.43	−10.94 ± 0.02	0.136
I18117-1753	18:14:39.21	−17:52:08.6	0.21 ± 0.066	31.6 ± 3.9	35.6 ± 9.08	0.42	4.11	1.94	1.64	1.03	−10.18 ± 0.051	0.138
I18139-1842	18:16:51.47	−18:41:39.5	0.22[a]	3.15 ± 0.17	39.36 ± 0.27	0.17	1.8	1.0	1.01	0.27	−11.04 ± 0.023	0.134
I18159-1648	18:18:54.84	−16:47:50.4	0.09	47.1 ± 3.5	20.13 ± 4.86	0.36	5.89	2.36	2.24	1.92	−10.49 ± 0.031	0.138
I18182-1433	18:21:09.03	−14:31:46.0	0.34[a]	12.24 ± 0.78	59.76 ± 0.63	0.4	2.82	1.61	1.64	0.52	−10.07 ± 0.027	0.130
I18236-1205	18:26:26.50	−12:03:53.4	0.16[a]	1.84 ± 0.16	27.13 ± 6.9	0.17	2.97	1.15	1.27	0.44	−11.57 ± 0.036	0.144
I18264-1152	18:29:14.91	−11:50:25.6	0.17 ± 0.061	19.4 ± 2.7	43.35 ± 4.27	0.55	4.88	1.78	1.35	1.04	−10.17 ± 0.057	0.137
I18290-0924	18:31:43.13	−09:22:32.9	0.39[a]	1.87 ± 0.24	84.15 ± 0.46	0.3	1.38	0.81	0.8	0.08	−10.78 ± 0.052	0.101
I18311-0809	18:33:53.54	−08:07:12.2	0.45[a]	3.35 ± 0.18	113.7 ± 0.19	0.32	2.3	1.44	1.47	0.33	−10.41 ± 0.023	0.096
I18316-0602 C1	18:34:21.17	−06:00:14.5	0.16[a]	28.3 ± 1.3	35.61 ± 12.71	0.29	8.83	4.23	3.88	7.48	−10.41 ± 0.02	0.093
C2	18:34:20.52	−05:59:33.6	0.16[a]	25.4 ± 2.5	43.5 ± 33.06	0.42	6.5	2.74	2.3	2.76	−10.46 ± 0.041	0.093
C3	18:34:20.52	−05:59:33.6	0.05 ± 0.131	6.6 ± 2.6	29.93 ± 5.4	1.05	7.78	2.48	1.91	2.37	−11.04 ± 0.144	0.093
I18341-0727	18:36:49.87	−07:24:53.6	0.45[a]	9.6 ± 1.1	112.5 ± 3.89	0.29	2.97	1.52	1.45	0.52	−9.96 ± 0.047	0.096
I18411-0338	18:43:46.11	−03:35:31.2	0.57[a]	5.23 ± 0.33	103.62 ± 0.06	0.23	1.82	1.08	1.18	0.22	−10.04 ± 0.027	0.115
I18434-0242	18:46:03.58	−02:39:24.7	0.39[a]	19.81 ± 0.49	97.65 ± 0.11	0.42	4.24	2.19	2.06	1.29	−9.78 ± 0.011	0.094
I18461-0113	18:48:41.74	−01:10:01.3	0.39[a]	14.65 ± 0.59	95.48 ± 0.34	0.46	2.53	1.58	1.63	0.35	−9.91 ± 0.017	0.094

Table A1 – *continued*

IRAS	RA (J2000)	DEC (J2000)	R_a (pc)	$\int F_\nu d\nu$ (Jy km s^{-1})	v (km s^{-1})	σ_v (km s^{-1})					log L_{SiO} ($L_\odot$)	σ (Jy beam^{-1})
						D_{min}	D_{max}	D_{mean}	D_{median}	D_{std}		
I18469-0132	18:49:33.05	−01:29:02.1	0.39[a]	4.57 ± 0.24	86.96 ± 0.12	0.17	1.72	1.04	0.92	0.18	− 10.42 ± 0.022	0.123
I18479-0005	18:50:30.63	−00:01:58.9	0.99[a]	8.42 ± 0.57	14.64 ± 3.11	0.45	2.84	1.83	1.85	0.46	− 9.35 ± 0.028	0.097
I18507p0110 C1	18:53:18.50	+ 01:15:01.2	0.08 ± 0.039	35.1 ± 6.1	58.9 ± 1.88	0.32	5.8	2.01	1.95	1.8	− 10.57 ± 0.07	0.126
C2	18:53:16.67	+ 01:15:11.1	0.08 ± 0.029	32.4 ± 3.9	61.56 ± 5.32	0.5	6.48	2.9	2.88	1.78	− 10.61 ± 0.049	0.126
C3	18:53:15.62	+ 01:14:20.1	0.12[a]	4.6 ± 1.4	54.97 ± 2.24	0.44	3.3	1.12	1.11	0.2	− 11.45 ± 0.115	0.126
I18507p0121 C1	18:53:18.02	+ 01:25:24.8	0.12[a]	48.7 ± 4.8	59.29 ± 8.86	0.23	4.78	2.29	2.19	2.27	− 10.43 ± 0.041	0.110
C2	18:53:17.90	+ 01:24:48.1	0.09 ± 0.03	29 ± 3.3	57.25 ± 7.38	0.67	7.04	2.71	2.44	2.13	− 10.65 ± 0.047	0.110
I18517p0437	18:54:14.50	+ 04:41:39.3	0.18[a]	8 ± 1	43.85 ± 0.23	0.23	1.43	0.72	0.7	0.09	− 10.85 ± 0.051	0.110
I18530p0215	18:55:33.42	+ 02:19:01.6	0.36[a]	0.41 ± 0.06	77.43 ± 3.21	0.17	3.22	0.97	0.67	0.62	− 11.55 ± 0.059	0.099
I19078p0901	19:10:13.24	+ 09:06:14.0	0.97 ± 0.099	278 ± 17	6.46 ± 2.0	0.88	6.91	3.81	4.0	2.27	− 7.97 ± 0.026	0.122
I19095p0930	19:11:53.85	+ 09:35:50.7	0.43[a]	18.7 ± 1	43.51 ± 0.18	0.95	3.32	2.16	2.22	0.4	− 9.67 ± 0.023	0.116
I19097p0847	19:12:09.04	+ 08:52:12.2	0.6[a]	6.51 ± 0.45	57.27 ± 0.38	0.31	2.83	1.6	1.76	0.56	− 9.83 ± 0.029	0.139

Notes. R_a: the linear radius of SiO clump. $\int F_\nu d\nu$: the integrated intensity of SiO clump. v: the velocity of SiO clump. σ_v: the velocity dispersion of SiO clump. L_{sio}: the luminosity of the SiO clump. σ: rms in one source.
[a] symbol after radius of SiO clump indicates that this SiO clump is unresolved by CASA.

Table A2. SiO (2-1) line parameters and clump properties in the region without clear detections.

IRAS	RA J2000	DEC J2000	R_a (pc)	$\int F_\nu d\nu$ (Jy km s^{-1})	v (km s^{-1})	σ_v (km s^{-1})	log L_{SiO} ($L_\odot$)	σ (Jy beam^{-1})
I12383-6128	12:41:18.18	−61:44:17.4	0.25[a]	1.08 ± 0.38	− 39 ± 2	1.3 ± 1.7	− 11.44 ± 0.13	0.14
I13080-6229	13:11:12.81	−62:45:02.1	0.58 ± 0.4	3.6 ± 1.4	− 35.7 ± 8.1	2.6 ± 6.6	− 10.79 ± 0.143	0.122
I13291-6229	13:32:32.54	−62:45:22.6	0.35 ± 0.18	2.35 ± 0.5	− 37.6 ± 3.8	0.99 ± 3.1	− 11.21 ± 0.08	0.125
I14050-6056	14:08:40.89	−61:11:18.4	0.28[a]	3.81 ± 0.99	− 53 ± 3	1.8 ± 2.4	− 10.85 ± 0.1	0.154
I14382-6017	14:42:03.76	−60:30:30.9	0.39 ± 0.59	3.6 ± 1.7	− 60.7 ± 2.6	1.2 ± 2.1	− 10.17 ± 0.095	0.153
I15254-5621	15:29:18.84	−56:31:38.4	0.28[a]	4.1 ± 1	− 68.5 ± 2.3	2.1 ± 1.8	− 10.69 ± 0.095	0.16
I15437-5343	15:47:33.06	−53:52:39.4	0.46	4.9 ± 1.4	− 83.1 ± 2.8	1.8 ± 2.3	− 10.69 ± 0.109	0.163
I15502-5302	15:54:03.32	−53:11:37.9	0.43 [a]	3.91 ± 0.74	− 92.4 ± 1.7	2 ± 1.4	− 10.38 ± 0.08	0.176
I16304-4710	16:34:05.19	−47:16:33.0	0.8 [a]	1.42 ± 0.48	− 62.3 ± 2.3	0.93 ± 1.9	− 10.24 ± 0.126	0.211
I16313-4729	16:34:54.38	−47:35:33.6	0.33 [a]	5.4 ± 1.2	− 74.3 ± 2.2	3 ± 1.8	− 10.42 ± 0.087	0.188
I16330-4725	16:36:43.25	−47:31:25.9	0.78 [a]	4.1 ± 1.2	− 71.4 ± 2.7	2.5 ± 2.2	− 9.81 ± 0.111	0.205
I16372-4545	16:40:54.07	−45:50:52.3	0.3 [a]	2.8 ± 0.5	− 58.2 ± 2.4	2 ± 2	− 10.82 ± 0.071	0.204
I16506-4512	16:54:13.35	−45:17:54.7	0.07 ± 0.05	5.74 ± 0.88	− 35.3 ± 1.9	3.8 ± 1.6	− 10.98 ± 0.062	0.181
I17136-3617	17:17:02.31	−36:20:49.4	0.09 [a]	2.64 ± 0.48	− 10.5 ± 2.7	2.8 ± 2.2	− 11.83 ± 0.073	0.176
I18110-1854	18:14:02.41	−18:53:14.1	0.39 ± 0.157	13.5 ± 4.1	38.5 ± 2.5	3 ± 2	− 10.32 ± 0.115	0.144
I18116-1646	18:14:36.17	−16:45:45.7	0.29 [a]	1.43 ± 0.52	48.6 ± 2.5	1.3 ± 2	− 11.16 ± 0.135	0.145
I18223-1243	18:25:11.12	−12:42:21.1	0.24[a]	1.31 ± 0.33	48.3 ± 2.4	2 ± 2	− 10.95 ± 0.076	0.168
I18228-1312	18:25:41.66	−13:10:11.6	0.29	4.24 ± 0.93	31.7 ± 2.7	0.77 ± 2.2	− 10.86 ± 0.086	0.148

Notes. R_a: The linear radius of SiO clump. $\int F_\nu d\nu$: The integrated intensity of SiO clump. v: SiO line central velocity. σ_v: The velocity dispersion of SiO clump. L_{sio}: The luminosity of the SiO clump. σ: rms in one source.
[a] symbol after radius of SiO clump indicates that this SiO clump is unresolved by CASA.

Table A3. SiO (2-1) line parameters and clump properties.

IRAS	L_{bol}/M	log$n$	[SiO]/[$H^{13}CO^+$]	D_d	H40α	Wing			outflow	type
						SiO	HCO^+	CS		
	($L_\odot M_\odot^{-1}$)	(cm^{-3})		(pc)						
I08076-3556	3.16	5.51	–	0.01	–	✓	–	–	✓	C
I08303-4303	25.12	5.4	0.41 ± 0.01	0.16	–	✓	✓	✓	✓	D
I08448-4343 C1	25.12	5.68	1.86 ± 0.07	0.06	–	✓	–	–	✓	D
C2	25.12	5.68	3.35 ± 0.37	0.08	–	✓	–	–	✓	D
I08470-4243	39.81	5.4	2.98 ± 0.1	0.02	–	✓	✓	✓	✓	C
I09002-4732 C1	158.49	5.78	0.74 ± -	0.2	✓	–	–	–	–	B
C2	158.49	5.78	–	0.15	✓	–	–	–	–	B
C3	158.49	5.78	–	0.08	✓	–	–	–	–	B
I09018-4816 C1	50.12	5.59	0.9 ± -	0.05	–	–	–	–	–	C
C2	50.12	5.59	–	0.48	–	–	–	–	–	D
I09094-4803	31.62	4.18	1.39 ± 0.16	0.93	–	–	–	–	–	D
I10365-5803	39.81	5.29	0.32 ± -	0.11	–	✓	✓	–	✓	D
I11298-6155	63.1	4.52	3.97 ± 0.19	0.37	✓	–	✓	✓	✓	A
I11332-6258	39.81	5.28	0.22 ± 0.05	0.03	–	–	✓	–	✓	C
I11590-6452	3.98	6.29	–	0.04	–	–	–	–	–	D

Table A3 – *continued*

IRAS	L_{bol}/M	log$n$	[SiO]/[$H^{13}CO^+$]	D_d	H40α	Wing			outflow	type
						SiO	HCO^+	CS		
	($L_\odot M_\odot^{-1}$)	(cm^{-3})		(pc)						
I12320-6122	398.11	3.61	0.7 ± 0.25	0.25	✓	✓	✓	✓	✓	B
I12326-6245	79.43	4.36	6.16 ± 0.12	0.07	✓	✓	✓	✓	✓	A
I12383-6128	5.01	4.32	0.99 ± 0.25	0.37	✓	–	–	–	–	B
I12572-6316	5.01	3.88	0.42 ± 0.05	0.12	✓	–	–	–	–	A
I13079-6218	39.81	4	4.77 ± 0.05	0.11	✓	✓	✓	✓	✓	A
I13080-6229	79.43	3.78	0.15 ± 0.01	0.17	✓	✓	–	–	✓	B
I13111-6228	50.12	3.77	0.09 ± -	0.04	✓	–	✓	–	✓	A
I13134-6242	31.62	4.45	3.04 ± 0.14	0.08	–	✓	✓	✓	✓	C
I13140-6226	7.94	4.42	1 ± -	0.05	–	✓	✓	✓	✓	C
I13291-6229	39.81	4.09	0.13 ± 0.01	0.38	✓	–	–	–	–	B
I13291-6249	31.62	3.6	1.85 ± 0.05	0.5	✓	✓	✓	✓	✓	B
I13295-6152	3.98	4.64	0.09 ± -	0.14	–	–	–	–	–	C
I13471-6120	79.43	4	0.62 ± 0.09	0.43	✓	✓	✓	✓	✓	B
I13484-6100	50.12	3.94	1.24 ± 0.05	0.14	–	✓	✓	✓	✓	C
I14013-6105	63.1	4.1	–	0.08	✓	–	–	–	–	A
I14050-6056	79.43	3.95	–	0.61	✓	–	–	–	–	B
I14164-6028	31.62	5.12	0.94 ± 0.04	0.04	–	–	–	–	–	C
I14212-6131	10.0	4.35	1.75 ± 0.12	0.36	–	✓	✓	✓	✓	D
I14382-6017	39.81	3.54	–	0.58	✓	–	–	–	–	B
I14453-5912	19.95	3.82	1.65 ± 0.45	0.33	✓	–	–	–	–	B
I14498-5856 C1	25.12	4.01	0.52 ± 0.01	0.12	–	–	✓	–	✓	D
C2	25.12	4.01	–	0.59	–	–	–	–	–	D
I15254-5621	100.0	3.87	–	0.35	✓	✓	–	✓	✓	B
I15290-5546	79.43	3.65	2.31 ± 0.03	0.18	✓	✓	✓	✓	✓	A
I15394-5358	6.31	4.53	1.75 ± 0.03	0.02	–	✓	✓	✓	✓	C
I15408-5356	100.0	4.16	3.85 ± 0.54	0.26	✓	✓	✓	✓	✓	B
I15411-5352 C1	63.1	4.05	0.22 ± -	0.08	✓	✓	–	✓	✓	B
C2	63.1	4.05	0.33 ± -	0.34	✓	–	–	–	–	B
I15437-5343	39.81	3.95	0.42 ± 0.11	0.11	–	–	–	–	–	C
I15439-5449 C1	25.12	4.1	0.77 ± 0.001	0.57	✓	–	–	–	–	B
C2	25.12	4.1	0.04 ± 0.003	0.41	✓	–	–	–	–	B
I15502-5302	125.89	3.65	1.04 ± 0.02	0.81	✓	–	–	✓	✓	B
I15520-5234 C1	79.43	4.34	16.45 ± 4.935	0.18	✓	✓	✓	✓	✓	B
C2	79.43	4.34	4.06 ± 0.005	0.06	✓	✓	–	✓	✓	A
I15522-5411	7.94	4.09	0.33 ± 0.002	0.04	–	✓	–	✓	✓	C
I15557-5215	5.01	4.07	4.81 ± 0.144	0.04	–	✓	✓	✓	✓	C
I15567-5236	158.49	3.76	0.38 ± 0.051	0.29	✓	✓	✓	✓	✓	B
I15584-5247	12.59	3.91	0.62 ± 0.043	0.4	–	✓	✓	✓	✓	D
I15596-5301	39.81	3.74	0.87 ± 0.033	0.34	–	–	–	–	–	C
I16026-5035	79.43	3.89	0.36 ± 0.07	0.31	–	–	–	–	–	D
I16037-5223	63.1	3.42	0.23 ± 0.028	0.1	✓	✓	✓	✓	✓	A
I16060-5146	79.43	4.23	–	0.08	✓	✓	✓	✓	✓	A
I16065-5158	50.12	3.87	1.5 ± 0.061	0.08	✓	✓	✓	✓	✓	A
I16071-5142	12.59	3.07	2.77 ± 0.022	0.08	–	✓	✓	✓	✓	C
I16076-5134	50.12	3.63	5.61 ± 0.016	0	–	✓	✓	✓	✓	C
I16119-5048	12.59	3.91	2.08 ± 0.141	0.07	–	✓	✓	✓	✓	C
I16164-5046	63.1	3.9	0.92 ± 0.091	0.05	✓	✓	–	✓	✓	A
I16172-5028 C1	63.1	4.08	1.27 ± 0.03	0.23	✓	✓	✓	✓	✓	B
C2	63.1	4.08	–	0.65	✓	–	–	✓	✓	B
C3	63.1	4.08	–	0.89	✓	✓	–	✓	✓	B
I16272-4837	12.59	4.04	2.53 ± 0.861	0.14	–	✓	–	✓	✓	D
I16297-4757	31.62	3.11	0.73 ± 0.055	0.14	✓	–	–	–	–	A
I16304-4710	25.12	3.7	0.26 ± 0.01	0.22	✓	–	–	–	–	A
I16313-4729	100.0	4.37	0.7 ± 0.04	0.13	–	–	–	–	–	C
I16318-4724	31.62	3.83	1.02 ± 0.042	0.09	–	✓	✓	✓	✓	C
I16330-4725	100.0	3.14	0.23 ± -	0.19	✓	–	–	–	–	A
I16344-4658	19.95	3.42	0.63 ± 0.028	0.24	–	✓	–	✓	✓	C
I16348-4654	10.0	3.87	2.14 ± 0.008	0.3	✓	✓	–	✓	✓	A
I16351-4722	50.12	4.3	2.27 ± 0.114	0.05	–	✓	–	✓	✓	C
I16372-4545	19.95	3.92	0.51 ± 0.02	0.2	–	–	–	–	–	D
I16385-4619	79.43	3.43	1.51 ± 0.126	0.06	✓	✓	✓	✓	✓	A

Table A3 – *continued*

IRAS	L_{bol}/M	log$n$	[SiO]/[$H^{13}CO^+$]	D_d	H40α	Wing			outflow	type
						SiO	HCO^+	CS		
	($L_\odot M_\odot{}^{-1}$)	(cm^{-3})		(pc)						
I16424-4531	15.85	4.12	0.74 ± 0.143	0.12	–	✓	–	✓	✓	D
I16445-4459	12.59	3.3	0.33 ± 0.07	0.39	–	–	–	–	–	D
I16458-4512 C1	7.94	3.76	4.39 ± 0.054	0.46	✓	✓	–	✓	✓	B
C2	7.94	3.76	–	0.47	✓	–	–	–	–	B
I16484-4603	100.0	4.39	2.65 ± 0.346	0.33	–	✓	–	–	✓	D
I16487-4423	25.12	3.6	1.31 ± 0.071	0.4	–	✓	–	–	✓	D
I16489-4431	7.94	3.96	1.09 ± 0.007	0.24	–	✓	–	✓	✓	D
I16506-4512	79.43	3.91	3.58 ± 0.67	0.55	✓	–	–	✓	✓	B
I16524-4300 C1	10.0	3.94	1.48 ± 0.13	0.3	–	–	–	–	–	D
C2	10.0	3.94	3.11 ± 0.262	0.47	–	–	–	–	–	D
C3	10.0	3.94	–	0.87	–	–	–	–	–	D
I16547-4247 C1	39.81	4.3	0.73 ± 0.06	0.08	–	✓	✓	✓	✓	C
C2	39.81	4.3	16.68 ± 7.892	0.43	–	✓	✓	✓	✓	D
I16562-3959 C1	316.23	4.24	0.8 ± 0.197	0.05	–	✓	✓	–	✓	C
C2	316.23	4.24	–	0.5	–	–	–	–	–	D
C3	316.23	4.24	–	0.47	–	–	–	–	–	D
I16571-4029	25.12	4.77	2.59 ± 0.083	0.02	–	✓	✓	✓	✓	C
I17006-4215	39.81	4.32	0.61 ± 0.087	0.14	✓	✓	–	–	✓	B
I17008-4040	39.81	3.31	0.57 ± 0.025	0.05	–	✓	–	–	✓	C
C2	39.81	3.31	42.78 ± 31.127	0.3	–	–	–	–	–	D
I17016-4124 C1	31.62	4.79	6.61 ± 0.19	0.09	–	✓	✓	✓	✓	D
C2	31.62	4.79	8.95 ± 1.579	0.08	–	✓	✓	✓	✓	D
I17136-3617	125.89	4.15	–	0.14	✓	✓	–	✓	✓	B
I17143-3700	63.1	3.0	0.19 ± 0.007	0.11	✓	–	–	✓	✓	A
I17158-3901	25.12	3.8	0.88 ± 0.02	0.04	–	✓	–	–	✓	C
I17160-3707 C1	79.43	4.03	1.16 ± 0.11	2.15	✓	✓	–	–	✓	B
C2	79.43	4.03	–	1.4	✓	–	–	✓	✓	B
C3	79.43	4.03	0.21 ± 0.024	3.35	✓	✓	–	✓	✓	B
I17175-3544 C1	50.12	5.08	1.9 ± 0.014	0.07	✓	✓	✓	✓	✓	B
C2	50.12	5.08	–	0.12	✓	✓	–	–	✓	B
C3	50.12	5.08	1.66 ± 0.274	0.29	✓	✓	✓	✓	✓	B
I17204-3636	19.95	4.18	0.28 ± 0.009	0.06	–	✓	–	✓	✓	C
I17220-3609	25.12	3.77	–	0.22	✓	✓	–	✓	✓	A
I17233-3606 C1	39.81	4.91	8.93 ± 0.712	0.15	✓	✓	✓	✓	✓	B
C2	39.81	4.91	2.91 ± 0.241	0.01	✓	✓	✓	✓	✓	A
C3	39.81	4.91	1.87 ± 0.235	0.22	✓	✓	–	✓	✓	B
I17244-3536	39.81	4.28	0.79 ± 0.182	0.16	✓	–	–	–	–	B
I17258-3637 C1	398.11	4.02	–	0.3	✓	✓	–	–	✓	B
C2	398.11	4.02	–	0.57	✓	–	–	–	–	B
I17269-3312	12.59	3.66	25.06 ± 2.55	0.04	–	✓	✓	✓	✓	C
I17271-3439	39.81	4.23	1.16 ± 0.094	0.1	✓	✓	–	✓	✓	A
I17278-3541 C1	19.95	4.64	–	0.16	–	✓	–	✓	✓	D
C2	19.95	4.64	–	0.15	–	✓	–	✓	✓	D
C3	19.95	4.64	1.32 ± 0.118	0.25	–	–	–	–	–	D
C4	19.95	4.64	–	0.21	–	✓	–	–	✓	D
C5	19.95	4.64	–	0.08	–	–	✓	✓	✓	D
C6	19.95	4.64	–	0.02	–	✓	✓	–	✓	C
I17439-2845	79.43	3.66	–	1.39	✓	–	–	✓	✓	B
I17441-2822 C1	15.85	4.81	0.6 ± 0.063	1.37	✓	–	–	–	–	B
C2	15.85	4.81	0.52 ± 0.046	0.96	✓	–	–	–	–	B
C3	15.85	4.81	0.28 ± 0.057	1.13	✓	–	–	–	–	B
C4	15.85	4.81	0.16 ± 0.017	1.26	✓	–	–	–	–	B
C5	15.85	4.81	–	0.36	✓	–	–	–	–	B
I17455-2800	63.1	3.7	3 ± 0.401	0.78	✓	✓	–	–	✓	B
I17545-2357	10.0	3.89	–	0.49	✓	–	–	–	–	B
I17589-2312 C1	10.0	4.17	–	0.45	–	–	–	–	–	D
C2	10.0	4.17	1.16 ± 0.105	0.23	–	–	–	–	–	D
I18032-2032	79.43	3.8	2.45 ± 0.016	0.24	✓	✓	✓	✓	✓	B
I18056-1952 C1	19.95	3.92	1.02 ± 0.017	0	✓	✓	✓	✓	✓	A
C2	19.95	3.92	2.08 ± 0.012	1.55	✓	✓	✓	✓	✓	B
C3	19.95	3.92	0.39 ± 0.026	0.73	✓	✓	–	–	✓	B

Table A3 – *continued*

IRAS	L_{bol}/M	log$n$	[SiO]/[$H^{13}CO^+$]	D_d	H40α	Wing			outflow	type
						SiO	HCO^+	CS		
	($L_\odot M_\odot{}^{-1}$)	(cm^{-3})		(pc)						
I18079-1756 C1	19.95	4.28	0.34 ± 0.026	0.05	–	–	–	–	–	C
C2	19.95	4.28	0.47 ± 0.099	0.26	–	–	–	–	–	D
I18089-1732	15.85	3.85	0.62 ± 0.069	0.03	–	✓	✓	✓	✓	C
I18110-1854	39.81	3.99	0.87 ± 0.13	0.35	✓	✓	–	–	✓	B
I18116-1646	100.0	3.73	0.09 ± -	0.18	✓	–	–	–	–	B
I18117-1753	12.59	4.09	1.52 ± 0.171	0.11	–	✓	✓	✓	✓	D
I18139-1842	251.19	4.15	0.6 ± 0.103	0.14	✓	✓	–	–	✓	B
I18159-1648	10.0	4.37	2.31 ± 0.259	0.03	–	✓	✓	✓	✓	C
I18182-1433	15.85	4.16	0.92 ± 0.08	0.04	–	✓	–	–	✓	C
I18223-1243	19.95	3.76	2.47 ± 0.68	0.81	–	–	✓	–	✓	D
I18228-1312	50.12	3.89	0.57 ± 0.24	0.19	✓	–	–	–	–	B
I18236-1205	3.98	4.14	0.71 ± 0.153	0.11	–	✓	–	✓	✓	D
I18264-1152	5.01	4.09	1.24 ± 0.015	0.14	–	✓	✓	✓	✓	D
I18290-0924	6.31	3.7	1.59 ± 0.245	0.24	–	–	–	–	–	D
I18311-0809	19.95	3.33	1.05 ± 0.091	0.12	✓	✓	✓	✓	✓	A
I18316-0602 C1	12.59	4.27	42.04 ± 1.271	0.09	–	✓	–	✓	✓	D
C2	12.59	4.27	1.53 ± 0.103	0.17	–	✓	✓	✓	✓	D
C3	12.59	4.27	–	0.07	–	–	–	✓	✓	C
I18341-0727	25.12	3.4	1.49 ± 0.084	0.45	✓	✓	✓	✓	✓	B
I18411-0338	25.12	3.42	0.42 ± 0.002	0.07	–	✓	–	–	✓	C
I18434-0242	125.89	3.7	1.04 ± 0.026	0.2	✓	✓	–	✓	✓	A
I18461-0113	19.95	4.27	0.73 ± 0.004	0.1	–	✓	✓	✓	✓	C
I18469-0132	63.1	4.12	0.34 ± 0.002	0.44	–	✓	–	–	✓	D
I18479-0005	79.43	3.65	0.56 ± 0.027	0.12	✓	–	–	–	–	A
I18507p0110 C1	39.81	4.88	0.75 ± 0.008	0.03	✓	✓	–	✓	✓	A
C2	39.81	4.88	–	0.24	✓	✓	✓	✓	✓	B
C3	39.81	4.88	–	0.18	✓	–	–	–	–	B
I18507p0121 C1	7.94	4.83	3.42 ± 0.067	0.01	–	✓	✓	✓	✓	C
C2	7.94	4.83	3.42 ± 0.399	0.12	–	✓	–	✓	✓	D
I18517p0437	50.12	5.43	0.5 ± 0.022	0.05	–	–	–	–	–	C
I18530p0215	25.12	3.84	0.13 ± 0.029	0.23	✓	✓	–	–	✓	B
I19078p0901	79.43	3.73	2.12 ± 0.02	0.16	✓	✓	✓	✓	✓	A
I19095p0930	100.0	4.29	0.8 ± 0.014	0.06	–	✓	✓	✓	✓	C
I19097p0847	15.85	3.5	1.18 ± 0.166	0.31	–	✓	✓	✓	✓	D

Note. L_{bol}/M: The bolometric luminosity to mass ratio. n: The particle number density. [SiO]/[$H^{13}CO^+$]: The integrated intensity ratio of SiO emission and $H^{13}CO^+$ emssion, and the - symbol indicates that the source has absorption features in their spectra. D_d: The separated linear distance between the central position of SiO clumps and the peak position of the 3 mm continuum emission. H40α column: the ✓symbol indicates that the SiO clump is associated with H40α emission. Wing columns: The ✓symbol represents that the SiO clump shows line wing emission; the sources with - symbol are excluded in analysis. outflow column: The ✓symbol indicates that the SiO clump is with outflow. Type column: A is the SiO clumps associated with both H40α emission and 3 mm continuum emission. B is the SiO clumps separated from both H40α emission and 3 mm continuum emission. C is the SiO clumps associated with 3mm continuum emission undetected H40α emission. D is the SiO clumps partly separated from 3mm continuum emission undetected H40α emission.

[1]*National Astronomical Observatories of China, Chinese Academy of Sciences, Beijing 100012, China*
[2]*School of Astronomy and Space Science, University of Chinese Academy of Sciences, Beijing 100049, People's Republic of China*
[3]*Shanghai Astronomical Observatory, Chinese Academy of Sciences, 80 Nandan Road, Shanghai 200030, Peoples Republic of China*
[4]*Key Laboratory for Research in Galaxies and Cosmology, Chinese Academy of Sciences, 80 Nandan Road, Shanghai 200030, Peoples Republic of China*
[5]*College of Marine Science and Technology, China University of Geosciences, Wuhan 430074, China*
[6]*Department of Astronomy, Yunnan University, Kunming, 650091, PR China*
[7]*Kavli Institute for Astronomy and Astrophysics, Peking University, 5 Yiheyuan Road, Haidian District, Beijing 100871, China*
[8]*Korea Astronomy and Space Science Institute, 776 Daedeokdaero, Yuseong-gu, Daejeon 34055, Republic of Korea*
[9] *Korea Astronomy and Space Science Institute, University of Science and Technology, Korea (UST), 217 Gajeong-ro, Yuseong-gu, Daejeon 34113, Republic of Korea*
[10]*Department of Astronomy, Peking University, 100871 Beijing, People's Republic of China*
[11]*Department of Physics, University of Helsinki, P.O. Box 64, Helsinki FI-00014, Finland*
[12]*Departamento de Astronomía, Universidad de Chile, Las Condes, Santiago 7550000, Chile*
[13]*Physical Research Laboratory, Navrangpura, Ahmedabad-380 009, India*
[14]*SOFIA Science Centre, USRA, NASA Ames Research Centre, MS-12, N232, Moffett Field CA 94035, USA*
[15]*Yunnan Observatories, Chinese Academy of Sciences, 396 Yangfangwang, Guandu District, Kunming 650216, China*
[16]*Chinese Academy of Sciences South America Center for Astronomy, National Astronomical Observatories, CAS, Beijing 100101, China*

[17]*Indian Institute of Science Education and Research (IISER) Tirupati, Rami Reddy Nagar, Karakambadi Road, Mangalam (P.O.), Tirupati 517 507, India*
[18]*School of Physics and Astronomy, Sun Yat-Sen University Zhuhai Campus, Tangjia, Zhuhai 519082, China*
[19]*Department of Astronomy, Eötvös Loránd University, Pázmány Péter sétány 1/A, H-1117 Budapest, Hungary*
[20]*Indian Institute of Space Science and Technology, Thiruvanan thapuram, 695 547 Kerala, India*
[21]*Jet Propulsion Laboratory, California Institute ofTechnology, 4800 Oak Grove Drive, Pasadena, CA 91109, USA*
[22]*S. N. Bose National Centre for Basic Sciences, Block-JD, Sector-III, Salt Lake City, Kolkata 700106, India*
[23]*Indian Institute of Astrophysics, II Block, Koramangala, Bengaluru 560034, India*

This paper has been typeset from a TEX/LATEX file prepared by the author.